



PhD Thesis

Faezeh Moshfeghifar

Hip Joint Finite Element Modeling

Department of Computer Science

Advisors: Kenny Erleben, Sune Darkner

Handed in: March 31, 2022

To my beloved brother, Amirhossein

University of Copenhagen
Faculty of Science
Department of Computer Science

Hip Joint Finite Element Modeling

Faezeh Moshfeghifar

Supervisors: Kenny Erleben
Sune Darkner

Abstract

Population-based finite element analysis of hip joint models enables us to study the effect of inter-subject variability on the simulation results. This approach is the dawn of computerized clinical trials and offers various contributions to improving current clinical treatment, the design of surgical simulators for virtual training, and optimizing hip implants.

Despite the broad application of population-based analyses, developing large-scale subject-specific models is a challenging task and requires extensive manual effort. Thus, most state-of-the-art studies are limited in the number of subjects, and the anatomical representations are often subjected to simplifications. For instance, the geometry of the hip joint area is replaced with simple shapes, or the bilateral variation in this area is ignored. Such assumptions may limit the reliability of the predicted results.

This thesis provides novel methods for developing finite element models that enable large-scale population-based assessment of hip joint behavior. We benefit from the power of computer science to improve the quality and automate the standard modeling approaches. We further employ our new pipeline to generate multiple subject-specific finite element models, including the bones and cartilages in the hip joint area. The subject-specific finite element models are clinically validated and have high-quality discretization with accurate geometries. These subject-specific models demonstrate different mechanical behavior across subjects within the same simulation scenario. Additionally, the simulation results vary between the left-hand and right-hand side of the body in each subject.

Our work is one of the largest model repositories concerning the number of subjects and regions of interest. We aim to empower researchers with free access to verified and reproducible computational models. Thus, our detailed research data, including the clinical images, the segmentation label maps, the finite element models, and software tools, are openly accessible on <https://diku-dk.github.io/libhip/>. In future work, we aim to add additional structures to our models and upscale the population size as a direct benefit of our approach.

Resumé

Populationsbaseret finit element-analyse af hoftedeledsmodeller gør os i stand til at studere effekten af subjekt-specifik variabilitet på simuleringresultaterne. Denne tilgang er begyndelsen til computeriserede kliniske forsøg og tilbyder forskellige bidrag til at forbedre den nuværende kliniske behandling, design af kirurgiske simulatorer til virtuel træning samt optimering af hofteimplantater.

På trods af den brede anvendelse af befolkningsbaserede analyser er udvikling af store fagspecifikke modeller en udfordrende opgave og kræver en omfattende manuel indsats. De fleste nye undersøgelser er således begrænset i antallet af emner, og de anatomiske fremstillinger er ofte udsat for forenklinger. For eksempel erstattes hoftedeledsområdet med simple former, eller den bilaterale variation i dette område ignoreres. Sådanne antagelser kan begrænse pålideligheden af de forudsagte resultater.

Denne afhandling giver nye metoder til at udvikle finit element-modeller, der muliggør storstilet populationsbaseret vurdering af hoftedeledsadfærd. Vi drager fordel af datalogiens kraft til at forbedre kvaliteten og automatisere processen for standard modellering. Vi anvender yderligere vores nye pipeline til at generere flere emnespecifikke finit element-modeller, herunder knogler og brusk i hoftedeledet. De emnespecifikke finit element-modeller er klinisk validerede og har diskretisering af høj kvalitet med nøjagtige geometrier. Modellerne demonstrerer forskellig mekanisk adfærd på tværs af emner inden for det samme simuleringsscenario. Derudover varierer simuleringresultaterne mellem venstre og højre side af kroppen i hvert emne.

Vores arbejde er et af de største modeldepoter vedrørende antallet af emner og områder af interesse. Vi sigter mod at give forskere fri adgang til verificerede og reproducerbare beregningsmodeller. Således er vores detaljerede forskningsdata, herunder de kliniske billeder, segmenteringsmærkekortene, finit element-modellerne og softwareværktøjer åbent tilgængelige på <https://diku-dk.github.io/libhip/>. I det fremtidige arbejde tilstræber vi at tilføje yderligere strukturer til vores modeller og opskalere befolkningsstørrelsen som en direkte fordel ved vores tilgang.

Acknowledgements

The journey to reach this stage far exceeds the Ph.D. for me. From the very beginning, I had the chance to learn from and enjoy this journey with many incredible researchers worldwide.

I want to thank my two supervisors, Kenny and Sune. The most important element in their supervision, in my view, was being able to see my potential, helping me maximize it, and making me believe in myself as a *researcher*. They taught me how to look into problems and introduced me to the tremendous capacity of computer science. I want to thank Kenny for bringing up the term *eye-candy* in research deliverables and elevating my dissemination skills. I am deeply grateful for their attempts to make our research environment a calm and creative space, and always having time for my concerns. I want to thank Susanne Claus, who inspired me as a persistent researcher and taught me how to adapt to changing circumstances.

I have had the privilege to be a part of the Marie Skłodowska-Curie European Training Network, awarded by the European Union's Horizon 2020 research and innovation program (grant agreement No. 764644). This program allowed me to travel and work with an active network of researchers from industry, healthcare, and academia. I have had the chance to learn from two brilliant scholars in my field: Stéphane Bordas and John Rasmussen, and be a member of a unique scientific team with 14 other early-stage researchers. I especially want to thank Christine Sarah Andersen for her constant caring concerning our team.

Next, I would like to extend my gratitude to all my colleagues at DIKU, especially those from my beloved RAINBOW office. Thank you all for our excellent brainstorming and for helping me feel at home in Denmark. I want to thank Mathias, who has been my greatest mathematician, who brought me an infinite amount of lovely moments.

Finally, I wish to express my sincere appreciation to my beloved family and friends. They never stopped sending beautiful vibes from Iran, Denmark, Canada, Belgium, the Netherlands, Luxembourg, and Australia. Though far away, the unconditional love from my parents, Soudabeh and Shahram, and my wonderful brother, Amirhossein, always made my heart warm and helped me go through the challenging moments of COVID-19.

Cheers,
Faezeh, Fayjhe, Fafa, Faaesee, Faazey

Contents

Abstract	i
Resumé	iii
Acknowledgements	v
1 Background	1
1.1 Anatomy of the hip joint area	1
1.2 Prospective of computational models	1
2 Introduction	5
2.1 Problem statement	5
2.2 Objectives	5
3 Summary and Future Work	9
Bibliography	12
List of Publications	16
A Auto-segmentation of Hip Joints using MultiPlanar UNet with transfer learning	19
B A direct geometry processing cartilage generation method for datasets with poor cartilage visibility	29
C LibHip: An Open-Access Hip Joint Model Repository suitable for Finite Element Method Simulation	45
D Contact modeling from images using cut finite element solvers	73
E Open-Full-Jaw: An open-access dataset and pipeline for finite element models of human jaw	75
F Velocity Skinning for Real-time Stylized Skeletal Animation	77

Chapter 1

Background

This chapter aims to introduce the anatomical terminology in this thesis to make sure they are accessible to an audience coming from different backgrounds. For a more thorough review, the reader is referred to [24]. We further give a brief introduction to computational models and their application in biomechanics.

1.1 Anatomy of the hip joint area

The hip joint forms an intricate organization of bones, muscles, cartilages, etc. Figure 1.1 illustrates the bones and cartilages in this region. The skeletal structure is made by the pelvic girdle and the two femurs. The pelvic girdle provides strength, stability and transfers the body weight to the femoral bones. This girdle is shaped by the two hip bones and the sacrum.

The sacrum reaches the hip bones in the *sacroiliac joint*, and the two hip bones connect at the *pubic symphysis*. Additionally, the acetabular part of the hip bone articulates within the femoral head to form the *hip joint*. The sacroiliac joint and the pubic symphysis provide stability and strength in the pelvic girdle, and the hip joint allows free rotation of the femur within the acetabulum cusp.

The connective cartilages cover the bones in these three joints to provide unhindered motion and cushion the bone surface. Figure 1.1 demonstrates how the lunate surface of the acetabulum and the entire femoral head, except the fovea pit, are covered by articular cartilages. This area resides other soft tissue, such as the ligaments, the hip joint capsule, and the muscles, which are out of the scope of this thesis.

1.2 Prospective of computational models

Modeling biological systems allows us to simulate their mechanical behavior without using the actual tissue. This method can simulate the load transfer across the hip joint and estimate the stress distribution in this area [21, 29]. Such simulations aid researchers in understanding the underlying mechanism of healthy hip joints and their mechanical alteration in complex disorders [19, 26, 29].

Computational modeling contributes to subject-specific applications in both surgical and non-surgical platforms. These models have the potential to predict

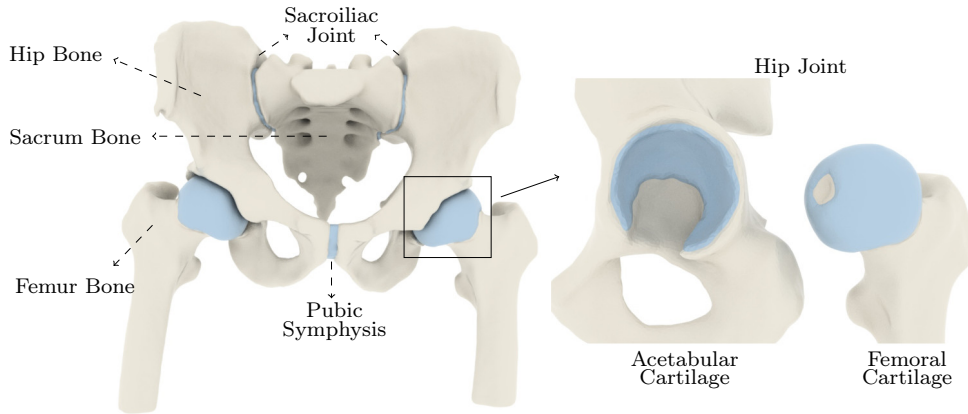


FIGURE 1.1: Overview of the anatomy around the hip joint; The skeletal structure consists of the hip, the sacrum, and the femur bones. The cartilage tissue in the sacroiliac joint, pubic symphysis and hip joint are shown in blue. We assume the sacroiliac and pubic symphysis as a single-piece cartilages, while the hip joint cartilage consists of two articular cartilages.

the outcome of surgical interventions and optimize clinical treatments [30]. They further contribute to the design of surgical simulators for virtual training [27] and are critical elements in the design of subject-specific implants, such as prosthetic hip components [3, 9, 28].

In a non-surgical setting, computational modeling is used to improve the performance and cost-effectiveness of the products in contact with the body. For example, the product designers of pelvic belts can benefit from analysis tools to integrate consumers and market feedback into the design of their products [22]. Moreover, analysis studies can potentially assess how pelvic skewness can alter the normal stress distribution on one side of the body and help reduce this pressure using subject-specific foot orthoses designs.

The public benefits of computerized clinical trials have been recognized by regulatory agencies and standard developing organizations. These institutions believe that patient care can be improved using computational analyses. For example, The Food and Drug Administration (FDA) and The American Society of Mechanical Engineers (ASME) have added computational simulations in their regulatory evaluation of medical devices (V&V40) and advise the industry to employ such tools in the research and product development schemes.

Computational models are mainly developed based on two approaches: 1) The musculoskeletal multibody modeling, and 2) Numerical modeling using the finite element method.

Musculoskeletal models present the geometry of the hip joint area with a chain of rigid body segments (bones) connected through points (joints). These models offer valuable insights into the hip joint movements and the muscle actions during daily activities and postures [5, 7]. However, the predicted results are limited to the joint points and do not extend to the entire geometry.

Numerical models are popular alternatives that utilize the principles of continuum mechanics and solve some of the issues arising from musculoskeletal models. The finite element method is a numerical approach to solve partial differential equations by discretizing the hip joint domain into a finite mesh [2]. Assessing the hip joint behavior through finite element analysis requires three main steps:

- The first step is to generate a proper approximation of the anatomical structures;
- Second, this anatomical information is transformed into surface and volume mesh representations to build a finite element model;
- Finally, the behavior of this model is studied under a chosen analysis scenario;

This thesis uses the finite element modeling approach to study the behavior of hip joint and introduces novel methods to improve the existing modeling pipeline.

Chapter 2

Introduction

This chapter introduces the difficulties of developing finite element models for simulation and explains how we contribute to taking a step further towards facilitating this procedure.

2.1 Problem statement

Developing hip joint finite element models starts with a proper approximation of the anatomical structures; Second, this anatomical information is transformed into a surface boundary and then filled with volume mesh elements; Finally, the behavior of the discretized models are studied under a specific analysis scenario.

The hip joint area exhibits multiple structures in contact which the shape and relative alignment of these structures vary among individuals. It is suggested that there is a significant variation in the hip joint contact mechanics due to the geometrical differences [8, 10]. Meanwhile, most studies assessing the hip joint behavior through finite element analysis are based on models from a *single* or a few subjects. This approach provides valuable information regarding that specific subject but does not account for the effect of the inter-subject variability and leaves uncertainties regarding the generality in the predicted results [25].

Adding *multiple* models in the simulations allows us to account for this variability [25] and observe its effect on the joint behavior. On the other hand, population-based studies are limited by clinical resources and the significant amount of time and manual effort to prepare large-scale hip joint models. In most cases, the final models are not freely available for research.

2.2 Objectives

Our overall objective in this thesis is to empower clinical researchers to have free access to multiple detailed and subject-specific finite element models of the hip joint area. We further want to deliver reliable alternatives to conventional techniques for developing such models. These tools mainly arise from looking at computational modeling from a computer science point of view and employing the potentials of geometry processing tools.

We want to make our research data, including the clinical images, the segmentation label maps, the finite element models, and software tools, accessible to researchers. These models allow them to use the benefits of computational modeling in research and investigate the importance of geometrical variance in the body's behavior.

Following, we will mention our contribution to each step of the finite element modeling workflow. In each paragraph, we refer to the motivation behind our related papers and explain why our geometry processing tools are superior to methods used by other works.

Level of anatomical details The anatomical representation of the hip joint area can be reconstructed at various levels of complexity, ranging from simplified phenomenological geometries to highly detailed and subject-specific models. Depending on the complexity of the problem, a few or all anatomical structures are added to the analysis.

In this thesis, we want to create detailed bilateral, and subject-specific models covering all the bones and cartilages explained in Chapter 1. The most challenging part of this method is that deriving large-scale subject-specific geometries from clinical images is time-consuming. Due to the tight space in the hip joint area, some structures, such as cartilages, are poorly visible in the clinical images.

Large-scale bone segmentation To reconstruct subject-specific bone geometries directly from images, we need *reliable* and *efficient* segmentation of the region of interest. Manual or semi-automated delineation of anatomical structures is generally reliable, but delineating large-scale datasets using these approaches is inefficient. This approach takes a very long time, and the process is highly limited by the image resolution and the annotator's expertise.

On the other hand, deep learning models are efficient ways to generate large-scale segmentations: These models are initially trained on a set of annotated images. Once the model is trained, it usually takes a short time to make predictions for new input. This method has been the motivation behind the work presented in Appendix A, which investigates the potential of UNET neural network architecture to segment the bony structures from a set of CT scans.

The result of this paper was an accurate approximation of the bone contours in 2D label maps and 3D geometry in multiple subjects. Further, the bone contours respect the inter-bone cavities, where cartilages reside. Thus, no two bones are connecting in the joint area.

Large-scale soft tissue reconstruction Delineating soft tissue from clinical images is challenging. This tissue, in general, is poorly visible in CT scan data, and for better visualization, one needs other image modalities such as MRI scans. Given the tight space in the hip joint, it is still challenging to identify the opposing cartilage interfaces in such modalities [11]. CT arthrography and manual traction are alternatives to increase the joint space, enhancing cartilage visibility at the cost of being an invasive intervention [12, 18].

In Appendix B and Appendix C we aim to reconstruct cartilage tissue in a much more efficient way. In these works, the main idea is that only the sufficiently close parts of bones in the joint have cartilages attached to them. We employ bone locality and geometry to create a fast geometry processing method that can generate subject-specific cartilages without directly segmenting them from clinical images.

The results from Appendix B generate subject-specific cartilages in the hip joint with non-uniform thickness. These cartilages have conforming interfaces with their underlying bones and form congruent interfaces between the articular boundaries. The high congruence level prevents potential spikes and peak stresses in the articulating surfaces, resulting in continuous stress distribution. We tend to improve the quality of the hip joint cartilage models in Appendix C and extend this work to creating cartilages for sacroiliac joint and pubic symphysis. The simple idea behind this approach can be extended to other joints in the body, such as the shoulder and knee joints (Appendix B) and the PDL layers attached to the teeth (Appendix E).

Surface and volume discretization The 2D segmented masks from clinical images are transferred to discretized 3D surface mesh. This surface boundary is then filled with volumetric elements, such as tetrahedrons [13, 14]. A common requirement in generating a volumetric domain is an explicit definition of the surface mesh. This surface should ideally be water-tight and without bad quality meshes. Unfortunately, this is rarely the case for segmented data from clinical images. The output geometries are dense and often self-intersecting. Traditionally, these imperfections need to be cleaned up before volumetric meshing, a laborious task, even when using state-of-the-art re-meshing tools [1].

A variety of approaches, such as delaunay meshing, advancing front, or grid stuffing, exist for volume mesh generation [14]. Most of these tools mesh the sub-domains of the hip joint complex separately, in a one-by-one approach. They do guarantee that the final volume meshes will share faces on adjacent surfaces and may introduce overlaps or gaps in the shared interfaces. Excessive overlaps may cause additional problems in the contact formulation, leading to invalid simulation results.

These issues motivated us to look for alternative discretization approaches to remove this manual and time-consuming step. In Appendix C, we seek a robust method to repair and preserve the mesh properties in the shared interfaces. To do so, we use a radically different approach first introduced in computer graphics [13]. This method generates volume meshes decoupled from the surface mesh quality and employs a multi-body volume mesh generation that simultaneously generates the whole complex's volume mesh, ensuring neither overlapping nor gaps in the interfaces. As a result the interface nodes are weld together in the meshing step, avoiding further contact definitions in the simulation setup.

Finite element method solvers Various research libraries, commercial codes, and software are available to solve elastic problems with the finite element method.

Most of these models are sensitive to user-defined solver settings unrelated to the physical quantities of interest. For example, changing the contact parameters and the time step size in these solvers can significantly affect the stability and accuracy of the predicted results and even lead to inverted elements.

One of the most critical user-defined parameters is mainly the contact setting between two geometries. The user must manually assign pre-defined contact surfaces in some contact models, such as those used in Abaqus and FEBio [16,23]. These two surfaces must have specific and different mesh resolutions regarding each other.

Calibrating the contact parameters for an optimal setting takes a long time in complex systems. Additionally, we want to minimize the amount of user interaction in this step so that the user does not need to manually define the potential surfaces that might come into contact during the simulation. These concerns motivated us in Appendix C to employ finite element solvers that are free of such requirements. In this paper, we introduce a solver which adopts the Incremental Potential Contact (IPC) formulation [6, 15], is robust to large deformations, and ensures no inverted elements using explicit line-search checks [15]. Our work is among the first works to employ this solver in the field of biomechanics [20].

Chapter 3

Summary and Future Work

This chapter summarizes the work presented in the appendices and discusses the possible future directions for this project. We keep this chapter brief and refer the reader to each appendix for more detail.

This thesis addressed the problems involved in the population-based finite element analysis of hip joint models. It used the computer science foundation to scale up the number of reconstructed models. In Chapter 1, we explained the importance of computational models and provided the anatomical and technical background to understand the terminologies used throughout the thesis. Chapter 2 outlined the challenges that are generally encountered during the development of finite element models and how each appendix contributed to providing solutions to these problems.

Appendix D was the very first time we reconstructed an anatomical structure from CT scans and tested this model in a simulation setup. This experience allowed us to understand the shortcoming of conventional methods in creating subject-specific computational models. One of the main bottlenecks was the extensive time needed to reconstruct a proper 3D surface mesh from clinical images. Even though the results of semi-automated segmentation were reliable, extending this to many datasets was not a feasible solution.

We raised this issue in Appendix A and looked into the existing problems regarding large-scale image-based bone reconstruction. We proposed an automated approach for generating multiple bone segmentation using very few annotated data for training the model. We show that the segmented models have accurate geometries and are suitable for simulation studies. This approach accelerates the process of image-based segmentation compared to manual or semi-automated methods and allows large-scale segmentation in a minimum amount of time.

Even though this approach facilitates the segmentation step, we still need to delineate the training dataset semi-automatically. Depending on the region of interest, this procedure may still take several days. A future direction for this work would be to scale up our test data and extract more anatomical components using this method.

In Appendix B, C, and E we targeted the subject-specific reconstruction of soft tissue. We combined multiple geometry processing tools to propose a novel

method to generate a subject-specific cartilage model without directly segmenting them from images. We only use the surface mesh of the bone models and create connective cartilages based on the distance and the anatomical information of the two involved bones at the joint. This novel approach enabled us to generate large-scale cartilages quickly, where the cartilages are poorly visible in the clinical images. The results were verified clinically and performed well in the simulation setup.

One limitation to our approach is that the cartilage generation algorithms are sensitive to the quality of the input bone models. Therefore any imperfection in the bone segmentation can affect the geometry of the cartilages. Further, even though this method is swift compared to direct cartilage segmentation, it still relies on geometry-related parameters that must be calibrated for each new subject. One future direction would be to decrease these parameters to speed up the process. We further would like to extend this approach to other joints and soft tissue. One example would be to adapt our expert system to generate knee joint cartilages and meniscus.

Appendix C is our most important paper where we provide multiple subject-specific finite element models of the hip joint area. We combine the outcome of Appendix A and Appendix B and feed new mesh generation and simulation tools to close up the improvement of the computational modeling pipeline. This work provides 11 subject-specific models of the hip joint area covering the bones and the cartilages. We employ multi-body volumetric meshing tools that mesh the whole complex simultaneously and generate high-quality discretization with conforming shared interfaces. The finite element solver is independent of unnecessary user-defined parameters, accelerating the simulations. These models allow scientists to perform population-based studies regarding the hip joint area and account for the inter-subject and bilateral variability in their population studies. Our research data are open-access and publicly available on <https://diku-dk.github.io/libhip/>.

The models in our repository are currently gender-biased and only belong to male subjects. Further, these models lack other soft tissue. Further work may be directed to add datasets from both genders and include more soft tissue in the modeling pipeline. Our finite element models are also biased by the position of the subjects during image acquisition. The subjects are in a supine position, and thus the relative alignment of the hip joint structures vary compared to a *neutral unloaded* joint. Future work can be extended to relocating these bones to remove such ill-posed conditions. We also want to investigate the possibility of removing surface mesh representation from the pipeline and going directly from segmentation label maps to volume mesh representations.

Now that we have a set of stable finite element models, our future question can be how to perform different simulations and use the results to understand the crucial elements when developing hip joint models. Post-processing the analysis results allow us to investigate the importance of age, geometrical differences in the behavior of hip joints. These data can be exploited to design protective orthoses for the older generation and optimize implants. Another exciting field

would be to investigate if our modeling approach could help clinicians diagnose a disease in its early stages and if we can modify our pipeline to develop finite element models for diseased datasets.

We want to apply our whole modeling pipeline to new anatomical structures in future work. Based on our estimations, if we want to develop 100 finite element models of a completely new location in the body, with all these improvements, we would need six months. This time would be spent training the automated segmentation model, modifying our cartilage generation pipeline, and setting up simulation scenarios. This is while developing such a repository with conventional models seems unfeasible.

Bibliography

- [1] Autodesk: Meshmixer. <http://www.meshmixer.com>, accessed: 2022-02-21
- [2] Baccouch, M.: A brief summary of the finite element method for differential equations. In: *Finite Element Methods and Their Applications*. IntechOpen (2021)
- [3] Chethan, K., Bhat, N.S., Zuber, M., Shenoy, B.S.: Finite element analysis of hip implant with varying in taper neck lengths under static loading conditions. *Computer Methods and Programs in Biomedicine* **208**, 106273 (2021)
- [4] Claus, S., Kerfriden, P., Moshfeghifar, F., Darkner, S., Erleben, K., Wong, C.: Contact modeling from images using cut finite element solvers. *Advanced Modeling and Simulation in Engineering Sciences* **8**(1), 1–23 (2021)
- [5] Damsgaard, M., Rasmussen, J., Christensen, S.T., Surma, E., De Zee, M.: Analysis of musculoskeletal systems in the anybody modeling system. *Simulation Modelling Practice and Theory* **14**(8), 1100–1111 (2006)
- [6] Ferguson, Z., Li, M., Schneider, T., Gil-Ureta, F., Langlois, T., Jiang, C., Zorin, D., Kaufman, D.M., Panozzo, D.: Intersection-free rigid body dynamics. *ACM Transactions on Graphics (SIGGRAPH)* **40**(4) (2021)
- [7] Fischer, M.C., Eschweiler, J., Schick, F., Asseln, M., Damm, P., Radermacher, K.: Patient-specific musculoskeletal modeling of the hip joint for preoperative planning of total hip arthroplasty: a validation study based on in vivo measurements. *PloS one* **13**(4), e0195376 (2018)
- [8] Harris, M.D., Anderson, A.E., Henak, C.R., Ellis, B.J., Peters, C.L., Weiss, J.A.: Finite element prediction of cartilage contact stresses in normal human hips. *Journal of Orthopaedic Research* **30**(7), 1133–1139 (2012)
- [9] Helgason, B., Pálsson, H., Rúnarsson, T.P., Frossard, L., Viceconti, M.: Risk of failure during gait for direct skeletal attachment of a femoral prosthesis: a finite element study. *Medical engineering & physics* **31**(5), 595–600 (2009)
- [10] Henak, C.R., Abraham, C.L., Anderson, A.E., Maas, S.A., Ellis, B.J., Peters, C.L., Weiss, J.A.: Patient-specific analysis of cartilage and labrum mechanics in human hips with acetabular dysplasia. *Osteoarthritis and cartilage* **22**(2), 210–217 (2014)

- [11] Henak, C.R., Anderson, A.E., Weiss, J.A.: Subject-specific analysis of joint contact mechanics: application to the study of osteoarthritis and surgical planning. *Journal of biomechanical engineering* **135**(2) (2013)
- [12] Henak, C.R., Carruth, E.D., Anderson, A.E., Harris, M.D., Ellis, B.J., Peters, C.L., Weiss, J.A.: Finite element predictions of cartilage contact mechanics in hips with retroverted acetabula. *Osteoarthritis and cartilage* **21**(10), 1522–1529 (2013)
- [13] Hu, Y., Schneider, T., Wang, B., Zorin, D., Panozzo, D.: Fast tetrahedral meshing in the wild. *ACM Transactions on Graphics (TOG)* **39**(4), 117–1 (2020)
- [14] Hu, Y., Zhou, Q., Gao, X., Jacobson, A., Zorin, D., Panozzo, D.: Tetrahedral meshing in the wild. *ACM Trans. Graph.* **37**(4), 60–1 (2018)
- [15] Li, M., Ferguson, Z., Schneider, T., Langlois, T., Zorin, D., Panozzo, D., Jiang, C., Kaufman, D.M.: Incremental potential contact: Intersection- and inversion-free large deformation dynamics. *ACM Transactions on Graphics* **39**(4) (2020)
- [16] Maas, S.A., Ellis, B.J., Ateshian, G.A., Weiss, J.A.: *Febio*: finite elements for biomechanics. *Journal of biomechanical engineering* **134**(1), 011005 (2012)
- [17] Rohmer, D., Tarini, M., Kalyanasundaram, N., Moshfeghifar, F., Cani, M.P., Zordan, V.: Velocity skinning for real-time stylized skeletal animation. In: *Computer Graphics Forum*. vol. 40, pp. 549–561. Wiley Online Library (2021)
- [18] Russell, M.E., Shivanna, K.H., Grosland, N.M., Pedersen, D.R.: Cartilage contact pressure elevations in dysplastic hips: a chronic overload model. *Journal of orthopaedic surgery and research* **1**(1), 6 (2006)
- [19] Salmingo, R.A., Skytte, T.L., Traberg, M.S., Mikkelsen, L.P., Henneberg, K.Å., Wong, C.: A method to investigate the biomechanical alterations in perthes' disease by hip joint contact modeling. *Bio-medical materials and engineering* **28**(4), 443–456 (2017)
- [20] Schneider, T., Dumas, J., Gao, X., Zorin, D., Panozzo, D.: *Polyfem*. <https://polyfem.github.io/> (2019)
- [21] SCIFERT, C.F., BROWN, T.D., PEDERSEN, D.R., HEINER, A.D., CALLAGHAN, J.J.: Development and physical validation of a finite element model of total hip dislocation. *Computer methods in biomechanics and biomedical engineering* **2**(2), 139–147 (1999)
- [22] Sichting, F., Rossol, J., Soisson, O., Klima, S., Milani, T., Hammer, N.: Pelvic belt effects on sacroiliac joint ligaments: a computational approach to understand therapeutic effects of pelvic belts. *Pain Physician* **17**(1), 43–51 (2014)

- [23] Smith, M.: ABAQUS/Standard User's Manual, Version 6.9. Dassault Systèmes Simulia Corp, United States (2009)
- [24] Standring, S.: Gray's anatomy e-book: the anatomical basis of clinical practice. Elsevier (2020)
- [25] Taylor, M., Bryan, R., Galloway, F.: Accounting for patient variability in finite element analysis of the intact and implanted hip and knee: a review. *International journal for numerical methods in biomedical engineering* **29**(2), 273–292 (2013)
- [26] Vafaeian, B., Zonoobi, D., Mabee, M., Hareendranathan, A., El-Rich, M., Adeeb, S., Jaremko, J.: Finite element analysis of mechanical behavior of human dysplastic hip joints: a systematic review. *Osteoarthritis and cartilage* **25**(4), 438–447 (2017)
- [27] Vaughan, N., Dubey, V.N., Wainwright, T.W., Middleton, R.G.: A review of virtual reality based training simulators for orthopaedic surgery. *Medical engineering & physics* **38**(2), 59–71 (2016)
- [28] Zeng, W., Liu, Y., Hou, X.: Biomechanical evaluation of internal fixation implants for femoral neck fractures: A comparative finite element analysis. *Computer Methods and Programs in Biomedicine* **196**, 105714 (2020)
- [29] Zhao, X., Chosa, E., Totoribe, K., Deng, G.: Effect of periacetabular osteotomy for acetabular dysplasia clarified by three-dimensional finite element analysis. *Journal of orthopaedic science* **15**(5), 632–640 (2010)
- [30] Zou, Z., Chávez-Arreola, A., Mandal, P., Board, T.N., Alonso-Rasgado, T.: Optimization of the position of the acetabulum in a ganz periacetabular osteotomy by finite element analysis. *Journal of Orthopaedic Research* **31**(3), 472–479 (2013)

List of Publications

- Appendix A Peidi Xu, Faezeh Moshfeghifar, Torkan Gholamalizadeh, and Michaels Bachmann Nielsen. “Auto-segmentation of Hip Joints using MultiPlanar UNet with Transfer learning” International Conference on Medical Image Computing and Computer Assisted Intervention (MICCAI) 2022.
- Appendix B Faezeh Moshfeghifar, Max Kragballe Nielsen, José D. Tascón-Vidarte, Sune Darkner, and Kenny Erleben. “A direct geometry processing cartilage generation method using segmented bone models from datasets with poor cartilage visibility” Computational Biomechanics for Medicine XVI (MICCAI Workshop) 2021.
- Appendix C Faezeh Moshfeghifar, Torkan Gholamalizadeh, Zachary Ferguson, Teseo Schneider, Michael Bachmann Nielsen, Daniele Panozzo, Sune Darkner, Kenny Erleben. “LibHip: An Open-Access Hip Joint Model Repository suitable for Finite Element Method Simulation” Under review at Journal of Computer Methods and Programs in Biomedicine. 2022
- Appendix D Susanne Claus, Pierre Kerfriden, Faezeh Moshfeghifar, Sune Darkner, Kenny Erleben, Christian Wong. “Contact modeling from images using cut finite element solvers” Journal of Advanced Modeling and Simulation in Engineering Sciences. 2021
- Appendix E Torkan Gholamalizadeh, Faezeh Moshfeghifar, Zachary Ferguson, Teseo Schneider, Daniele Panozzo, Sune Darkner, Masrour Makaremi, François Chan, Peter Lampel Søndergaard, Kenny Erleben. “Open-Full-Jaw: An open-access dataset and pipeline for finite element models of human jaw” Under review at Journal of Computer Methods and Programs in Biomedicine. 2022
- Appendix F Damien Rohmer, Marco Tarini, Niranjana Kalyanasundaram, Faezeh Moshfeghifar, Marie-Paule Cani, Victor Zordan “Velocity Skinning for Real-time Stylized Skeletal Animation” EuroGraphics. 2021

Appendix A

Auto-segmentation of Hip Joints using MultiPlanar UNet with transfer learning

The following chapter presents the article:

Peidi Xu, Faezeh Moshfeghifar, Torkan Gholamalizadeh, and Michaels Bachmann Nielsen. “Auto-segmentation of Hip Joints using MultiPlanar UNet with Transfer learning” Under review at Medical Image Computing and Computer Assisted Intervention (MICCAI) 2022.

Automated segmentation is an efficient approach to generating large-scale segmentations. Even though these models provide accurate 2D segmentation label maps, there is still a lack of quality assessment of these results’ 3D surface mesh representation. Typically, contouring methods convert a segmentation label map into a surface mesh representation. The surface mesh will be slightly enlarged during this procedure, often by half a voxel size. This implies that the resulting segmentation of bones with shared interfaces may be penetrating each other or have gaps. Further, the arrangement of two labeled pixels concerning each other may result in self-intersection in the 3D geometry. All these imperfections can bring challenges to the simulation scheme and result in erroneous predictions of the hip joint.

This paper was our improvement in the first step of the modeling pipeline. In this work, we investigated the potential of deep learning models in providing large-scale accurate bone geometries suitable for finite element modeling. This approach reduced the manual workload of segmentation to only a few annotated data in the training dataset. The accurate approximation of the bone geometries in this work details the shape and boundaries of bones, and further, the label maps identify the inter-bone cavities in each joint. Thus, no two bones are connecting in the joint space. The surface mesh representation of these label maps is guaranteed to be manifold, without inverted elements, and without the staircase effects.

Auto-segmentation of Hip Joints using MultiPlanar UNet with Transfer learning

Peidi Xu¹, Faezeh Moshfeghifar¹, Torkan Gholamalizadeh^{1,3}, Michael Bachmann Nielsen², Kenny Erleben¹, and Sune Darkner¹

¹ Department of Computer Science, University of Copenhagen, DK
darkner@di.ku.dk

² Department of Diagnostic Radiology, Copenhagen University Hospital, DK

³ 3Shape A/S, Copenhagen, DK

Abstract. Accurate geometry representation is essential in developing finite element models. Although generally good, deep-learning segmentation approaches with only few data have difficulties in accurately segmenting fine features, e.g., gaps and thin structures. Subsequently, segmented geometries need labor-intensive manual modifications to reach a quality where they can be used for simulation purposes. We propose a strategy that uses transfer learning to reuse datasets with poor segmentation combined with an active learning step where fine-tuning of the data results in anatomically accurate segmentations suitable for simulations. We use a modified MultiPlanar UNet that is pre-trained using inferior hip joint segmentation combined with a dedicated loss function to learn the gap regions and post-processing to correct some tiny inaccuracies on symmetric classes due to rotational invariance. We demonstrate this robust yet conceptually simple approach applied with clinically validated results on publicly available computed tomography scans of hip joints.

Keywords: Segmentation · Finite Element modeling · Transfer learning

1 Introduction

Precise segmentation of medical images, such as computed tomography (CT) scans, is widely used for generating finite element (FE) models of humans used for patient-specific implants [2]. A requirement in generating FE models is to have a proper geometrical representation of the anatomical structures [9]. In our case, an *accurate* segmentation of the hip joint (HJ) should essentially detail the shape and boundaries of the femur and the pelvic bones and identify the inter-bone cavities. The segmented geometries should be closed, non-intersecting, and without spikes. As manual segmentation is labor-intensive and time-consuming [9], there is a need for automated segmentation tools that can generate accurate FE models.

Convolutional Neural Networks with encoder-decoder structures are widely used for auto semantic segmentation, among which the most successful one is the UNet structure [10]. The architecture uses skip connection on high-resolution

2 P. Xu et al.

feature maps in the encoding path to include more fine-grained information. Although more recent models are proposed on segmenting natural images, e.g., DeepLabV3+, UNet still provides some of the best 3D medical image segmentation results [1]. Therefore, the variation of UNet, e.g., 3D UNet, is a straightforward way to segment 3D medical data like CT scans and has shown its state-of-the-art performance [3]. Applying 3D convolutions directly to large 3D images may overflow memory. Therefore, 3D models are usually trained on small patches, which results in a limited field of view and subsequent loss of global information. As an alternative with far less memory usage, the MultiPlanar UNet (MPUNet) model was proposed by Perslev et al. [8] which uses a 2D UNet to learn representative semantic information.

Most studies on auto-segmentation of the HJs focus on designing more powerful neural networks that separate anatomical structures with little manual intervention [12, 13]. These studies focus primarily on the bone morphology and not on the inter-bone gaps. The consequence is that although they reach fairly high Dice scores, the segmentation results are anatomically inaccurate and are unsuitable for generating HJ 3D models. This limits the usability of the existing deep learning models for FE simulations [7].

We require the deep learning models to provide anatomically correct segmentation of the bones and the existing gap in the HJ as shown in Fig. 1 [12, 13]. Due to the limited number of accurate training data, we propose a deep learning-based strategy for enhancing publicly available poorly annotated scans using only a few accurately segmented data to learn an accurate model and in our case the gap regions in HJ. Besides using the idea of MultiPlanar, our backbone model is a standard UNet with batch normalization. Therefore, the proposed pipeline is both parameter and memory efficient.

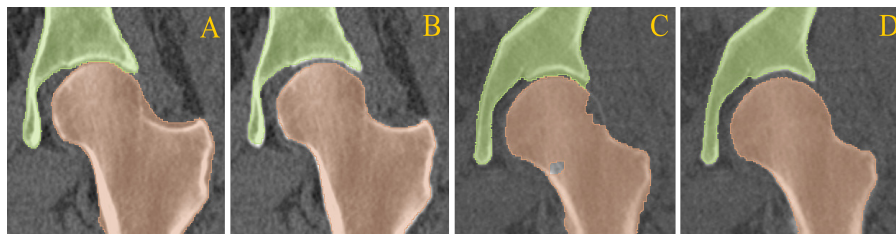


Fig. 1: Illustration of gap generation: Inferior ground truth of a training image from public dataset (A) and results by fine-tuned model (B). Results on a test image with model trained only on public dataset (C) and fine-tuned (D)

To enforce the cartilage gap with few annotated data, we apply MPUNet with a dedicated loss function penetrated more on the gap regions combined with transfer learning and a post-processing step. Our framework uses an interactive learning pipeline involving pre-training MPUNet on a public dataset with inferior HJ segmentation to learn general semantic features of the bones [5]. The model

Title Suppressed Due to Excessive Length 3

is then fine-tuned using a few highly accurate segmentation to learn the correct labeling of the gaps. We show that our proposed approach allows the model to learn the gap and generate anatomically accurate segmentation, using the pre-trained model and only four accurate segmentations for fine-tuning. Our work is validated on a set of HJs from which we construct FE models and report the Dice with the manually corrected segments used for biomechanical models.

2 Method

Our strategy for accurate HJ segmentation with very few accurate training images relies on the following: (i) we use the idea of MPUNet that segments 3D medical images using 2D models while preserving as much spatial information as possible by segmenting different views of the data. (ii) we use a relatively simple yet powerful backbone model for performing the segmentation to avoid overfitting and memory issues. (iii) we pre-train the model using publicly available datasets with poor labels, which are then fine-tuned with a very small set of accurately annotated data. (iv) we use a dedicated weighted distance loss to enforce the gap between the bones. (v) we introduce a post-processing step that solves the internal problem of MPUNet on images with symmetric features and can be generalized to other segmentation tasks involving symmetric and disconnected groups.

Model: As a baseline model, we use the MPUNet proposed by Perslev et al. [8] to segment the 3D HJs using 2D UNet while preserving as much 3D spatial information as possible by generating views from different perspectives. During training, the model $f(x; \theta)$ takes a set 2D image slices of size $w \times h$, from different views, and outputs a probabilistic segmentation map $P \in w \times h \times K$ for K classes for each slice. A standard pixel-wise loss function is then applied for back-propagation. Our experiment uses a standard categorical cross-entropy loss augmented by the weighted distance map. We found no improvement using a class-wise weighted cross-entropy loss or the dice loss. In the inference phase, we run 3D reconstruction in each view separately over the segmentation results on all the parallel slices to get the volume back. This results in a volume probability map of size $P \in m \times w \times h \times K$ for each view. Unlike original MPUNet [8] which suggests training another fusion model using validation data, we simply use majority voting by summing over results from different views and performing an argmax. This strategy achieves good results on the validation data.

Transfer Learning: The accurate segmentation and fast convergence rely partially on pre-training the model using publicly available datasets with poor labeling, which is subsequently fine-tuned with a small set of accurate training data. We detail two modifications that differ from standard transfer learning settings. First, we also transfer the weight in the last softmax layer because we work on exactly the same classes as before. Our experiment has shown that this results in a much faster convergence. Then, instead of freezing encoder and only fine-tuning decoder, it is necessary to explicitly learn encoder to detect the gap, as the gap must be encoded correctly first.

4 P. Xu et al.

Weighted Distance Map: For the model to be fined-tuned to learn the gap between the bones, we enforce a voxel-wise weight-map $w(x)$ to the loss function based on the distances to the border of the foreground classes. This strategy was initially suggested in the original UNet paper, which we employ in a modified version for 3D data [10, 8]. We define $w(x)$ as follows,

$$w(x) = w_c(x) + w_0 \cdot e^{-\frac{(d_1(x)+d_2(x))^2}{2\sigma^2}} \quad (1)$$

where d_1 and d_2 denotes the distance to the border of the nearest foreground class and the second nearest foreground class respectively. We follow original UNet paper and set $w_0 = 10$ and $\sigma = 5$. $w_c : \Omega \rightarrow R$ is used to balance the class frequencies, which we do not enforce, thus we set $w_c = 1$ for every c.

During fine-tuning, the corresponding slice of the 3D weight map is sampled together with the images and labels. We apply an element-wise multiplication of the weight map with the cross-entropy loss of predictions and labels on each pixel before reduction. Fig. 2 (left & middle) shows an example training slice. Note that we do not plot the prediction since it consists of multi-class probabilities.

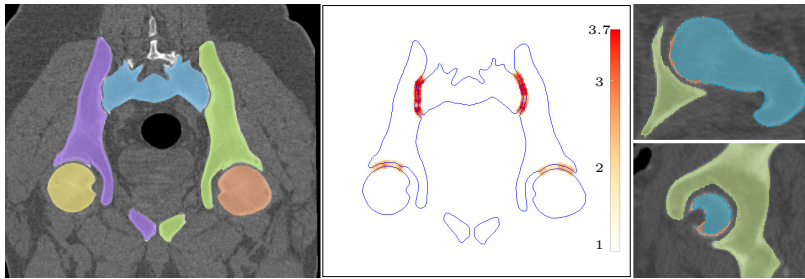


Fig. 2: (left) A sample training slice of true labels overlaid on top of raw image. (middle) Corresponding weight map computed with Eq. (1) overlaid on top of label boundaries. (right) Results of training with weight map calculated over eroded labels (orange contour), which shows a smoother and more complete contour near the boundaries than the results trained without erosion (blue contour).

We have noticed that the model is prone to overfitting to the gap, producing a broader gap than usual if we use higher weights only to the gap regions in Eq. (1) because it only penalizes on the gap region. Instead, we would like to assign more weight to the boundaries on the two sides of the gap to avoid false negatives. Thus, we apply a mathematical erosion to the labels over a ball with a radius of 3 voxels before calculating the weight map. This operation ensures that both the gap and the boundaries near the borders get assigned higher weights, as demonstrated in Fig. 2 (middle). To compensate for the increased value of $d_1 + d_2$ introduced by the erosion, we double w_0 to 20.

Sampling Strategies: Sampling and interpolation are necessary to retrieve corresponding 2D slices from a 3D medical image viewed from a random orientation

Title Suppressed Due to Excessive Length 5

other than the standard RAS axes. We follow the idea in [8] by sampling pixel with dimension $d \in \mathcal{Z}^+$ on isotropic grids within a sphere of diameter $m \in \mathcal{R}^+$ centered at the origin of the scanner coordinate system in the physical scanner space. We differ in that these two numbers are chosen as the 75 percentile across all axes and images during training but as maximum value during inference. Please refer to Supplementary material for the effect of doing so.

Post-Processing: Although MPUNet is both parameter and memory efficient, the model is trained on 2D slices with a possibly limited field of view near the boundaries. Furthermore, the model is trained to segment the input viewed from different perspectives by sampling from planes of various orientations. This introduces some rotational invariance to the training and makes it hard to distinguish between symmetric classes with very similar semantic features. For example, it is hard to be consistent with the left and right femurs when viewing the input from various perspectives. Therefore, in the results, some part of the left femur and pelvis near the boundaries is mis-classified as the right femur and pelvis respectively, and vice versa, as shown in Fig. 3.

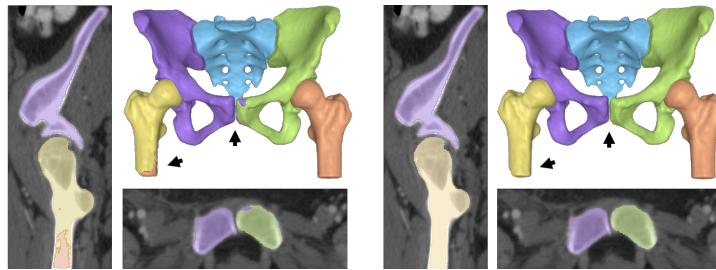


Fig. 3: Segmentation (left) with post-processing (right) where falsely predicted symmetric groups are recovered.

In order to solve this problem automatically, we propose a symmetric connected component decomposition. We only keep the largest connected component for each symmetric class pair while assigning the corresponding symmetric class value to all the other components. By doing this instead of just removing small components, those parts predicted as the left femur on the right femur are mapped correctly to the right femur, and vice versa. We then apply a standard connected component decomposition while keeping only the largest connected component for each foreground class to remove floating points of each class (false positives). A final 3D closing is applied to remove holes inside each class.

We acknowledge that our post-processing is highly task-specific but could also be generalized to other segmentation tasks with symmetric classes that share similar semantic features and are disconnected from each other.

6 P. Xu et al.

3 Data and Experiments

We use 35 CT scans from The Cancer Imaging Archive [4]. The dataset consists of subjects scanned in a supine position with no diagnosed diseases related to the HJ. For the pre-training step, we use 10 scans and their associated inferior segmentations from a publicly available dataset of *segmented CT pelvis scans with annotated anatomical landmarks* (CTPEL) [5, 12]. We only use two scans with accurate segmentation to fine-tune the model in the first place. In the next step, two other unseen scans are used to get the segmentation results of the model. Then, we manually correct these two results and fine-tune the model again. The second fine-tuning process could be re-iterated, but a total of four images is sufficient to obtain accurate results. We evaluate the segmentation results of our approach with minimal required accurate fine-tuning data. A clinical expert evaluated the segmentation results of the 21 test cases.

Pre-processing: We pre-process the data by first filtering out all negative values in the volume because both bones and cartilages should have positive Hounsfield unit values. We then apply a standardization based on the equation $X_{\text{scale}} = (x_i - x_{\text{mean}}) / (x_{75} - x_{25})$, where x_{25} and x_{75} are the 1st and 3rd quartiles respectively. This removes the median and scales the intensity based on quartiles and is more robust to outliers. No other pre-processing is applied to avoid any manual errors that can easily propagate in a neural network.

Experimental Setup: The network is trained on NVIDIA GeForce RTX 3090 with a batch size of 10 using the Adam optimizer for 40 epochs with a learning rate of $1e-5$ and reduced by 10% for every two consecutive epochs without performance improvements. We apply early stopping if the performance of five consecutive epochs does not improve. Pre-training takes approximately one day, while fine-tuning takes about six hours to reach convergence.

Augmentations: We apply Random Elastic Deformations to generate images with deformed strength and smoothness [11]. The augmentations are generated on the fly during the training process, and following MPUNet we assign a weight value of $1/3$ for the deformed samples [8].

4 Results

To have suitable geometries for FE models, the auto-segmentation framework must separate bones and generate accurate results near the boundaries, which is essential for generating cartilage layers for HJ. Therefore, any standard evaluation metric such as the Dice score could be misleading. Hence, our results, including the bone outlines and the existing gap in the joints, are first validated by a senior consultant radiologist as our clinical expert.

The clinical expert initially scrolls through all the segmented slices for each subject and verifies the bone contours and the gaps between the pelvic and femoral bones. Then, he verifies the anatomical shape and smoothness of the reconstructed 3D model. This procedure justifies the validation of our method in obtaining precise HJ geometries.

Title Suppressed Due to Excessive Length 7

Fig. 3 illustrates the results of the fined-tuned model on the test set and demonstrates the effect of post-processing mentioned above. Because of the limited field of view and being viewed from different perspectives, some symmetric classes are misclassified near the boundaries and are successfully recovered by the post-processing step. It can be seen that with the distance weight applied to loss, the model can detail the gap accurately. The final result is accurate and requires little or no human intervention for subsequent simulation experiments, e.g., FE analysis. Results in 3D are available in the GitHub repo mentioned in Supplementary material. As an example, we have generated the cartilage geometry on the segmented HJ with a method proposed by [6] to analyze the stress distributions as shown in Fig. 4. The results show a smooth stress pattern indicating that our method’s output is suitable for use in FE simulations.

	Dice \uparrow	GapDice \uparrow	HD \downarrow
Ours	98.63 \pm 0.56	96.47 \pm 1.60	3.67 \pm 1.13
NoPretrain	97.82 \pm 0.59	95.13 \pm 1.42	5.26 \pm 2.10
NoWeight	98.12 \pm 0.47	94.35 \pm 2.19	4.58 \pm 1.50
3DUNet	93.36 \pm 1.84	87.48 \pm 3.01	7.02 \pm 1.09
NoFineTune	93.22 \pm 1.33	84.16 \pm 3.41	12.07 \pm 6.82

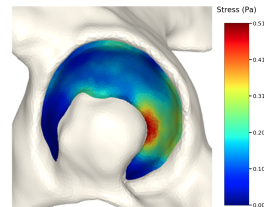


Table 1: Test Results of our model compared with various design choices. Note that HD is in the scale $\#voxels$

Fig. 4: Smooth von Mises stress pattern

4.1 Numerical Validation and Ablation Study

Although numerical results could be misleading regarding the final FE simulations, we include them as a validation and ablation study of our several design choices. Table 1 shows the numerical validations on the test set, including nine images with manually corrected ground truth segmentations. We test the performance by varying one of the design choices each time while keeping the others fixed. (i) The strategy mentioned in Section 2 (ours), (ii) Training without using ten inaccurate public data (NoPretrain), (iii) Training without enforcing distance weight map (NoWeight), (iv) Using 3D UNet as the backbone (3DUNet), (v) Using only ten inaccurate public data without fine-tuning (NoFineTune).

Besides the standard Dice score, we are especially interested in the surface and gap regions. Therefore, two more evaluation metrics are introduced here. We use Hausdorff distance (HD) as surface measurement by computing the largest distance between the result and the nearest point on the ground truth.

$$HD(P, Y) = \max(\max_{p \in P} \min_{y \in Y} \|p - y\|_2, \max_{y \in Y} \min_{p \in P} \|p - y\|_2) \quad (2)$$

We also propose a GapDice in Eq. (3) to measure the average Dice score between the segmentation result and the ground truth only around the gap

8 P. Xu et al.

regions. Given the segmentation results P and ground truth segmentation Y , we compute the Euclidean distance transformation map Y_d of Y , corresponding to the $d_1 + d_2$ term from Eq. (1). The gap region G is defined as the locations where $Y_d < \epsilon$. The Dice score between P and Y is calculated in the standard way inside G . Here we choose $\epsilon = 10$ as we found it to be a good indicator of the gap region and boundary locations. Fig. 2 (right) shows the region computed by eroded labels, which is also an indication of such regions. Please refer to Supplementary material for a detailed illustration of such regions.

$$\text{GapDICE}(P, Y) = \frac{2 * |P \cap Y \cap G|}{|P \cap G| + |Y \cap G|} \quad (3)$$

The results show that MPUNet (all the first three models) works significantly better than 3D UNet for a data scarcity setting. Our pipeline outperforms in all three metrics. Especially, although the difference of the Dice score is not significant, pretraining on inaccurate data and enforcing the weight map shows a significantly better GapDice score and HD, which is vital for further simulation.

5 Conclusion

We have presented an auto-segmentation framework for accurate segmentation from CT scans considering the bone boundaries and the inter-bone cavities. Our framework uses a modified version of MPUNet pre-trained on a public dataset with coarse segmentation and fine-tunes with very few data with accurate segmentations. In addition, we improve the performance of MPUNet on symmetric classes by symmetric connected component decomposition. We demonstrate that our simple yet robust model can detail crucial features, such as the gap where the cartilage resides.

This work is tested out on HJ CT scans and provides anatomically accurate segmentation, which has both been verified by a clinical expert and shown superior numerical results, reaching an overall Dice score above 98% and above 96% around gap regions. Our method can be used to enhance anatomically incorrect and poorly annotated datasets with a few accurately annotated scans. The FE analysis performance test shows that the generated models produce smooth stress patterns without any geometry-related artifacts. Thereby, the segmentation result of this work can be used for generating FE models with little or no manual modifications.

6 Acknowledgements

This project has received funding from the European Union’s Horizon 2020 research and innovation programme under the Marie Skłodowska-Curie grant agreement No. 764644. This paper only contains the author’s views, and the Research Executive Agency and the Commission are not responsible for any use that may be made of the information it contains.

Title Suppressed Due to Excessive Length 9

References

1. Liang-Chieh Chen, Yukun Zhu, George Papandreou, Florian Schroff, and Hartwig Adam. Encoder-decoder with atrous separable convolution for semantic image segmentation. In *Proceedings of the European conference on computer vision (ECCV)*, pages 801–818, 2018.
2. Xiaojun Chen, Lu Xu, Yiping Wang, Yongqiang Hao, and Liao Wang. Image-guided installation of 3d-printed patient-specific implant and its application in pelvic tumor resection and reconstruction surgery. *Computer Methods and Programs in Biomedicine*, 125:66–78, 2016.
3. Özgün Çiçek, Ahmed Abdulkadir, Soeren S Lienkamp, Thomas Brox, and Olaf Ronneberger. 3d u-net: learning dense volumetric segmentation from sparse annotation. In *International conference on medical image computing and computer-assisted intervention*, pages 424–432. Springer, 2016.
4. Kenneth Clark, Bruce Vendt, Kirk Smith, John Freymann, Justin Kirby, Paul Koppel, Stephen Moore, Stanley Phillips, David Maffitt, Michael Pringle, et al. The cancer imaging archive (tcia): maintaining and operating a public information repository. *Journal of digital imaging*, 26(6):1045–1057, 2013.
5. Bryan Connolly and Chunliang Wang. Segmented CT pelvis scans with annotated anatomical landmarks, 2019.
6. Faezeh Moshfeghifar, Max Kragballe Nielsen, José D. Tascón-Vidarte, Sune Darkner, and Kenny Erleben. A direct geometry processing cartilage generation method using segmented bone models from datasets with poor cartilage visibility, 2022.
7. Takashi Nishii, Nobuhiko Sugano, Yoshinobu Sato, Hisashi Tanaka, Hidenobu Miki, and Hideki Yoshikawa. Three-dimensional distribution of acetabular cartilage thickness in patients with hip dysplasia: a fully automated computational analysis of mr imaging. *Osteoarthritis and Cartilage*, 12(8):650–657, 2004.
8. Mathias Perslev, Erik Bjørnager Dam, Akshay Pai, and Christian Igel. One network to segment them all: A general, lightweight system for accurate 3d medical image segmentation. In *International Conference on Medical Image Computing and Computer-Assisted Intervention*, pages 30–38. Springer, 2019.
9. Sander Poelert, Edward Valstar, Harrie Weinans, and Amir A Zadpoor. Patient-specific finite element modeling of bones. *Proceedings of the Institution of Mechanical Engineers, Part H: Journal of Engineering in Medicine*, 227(4):464–478, 2013.
10. Olaf Ronneberger, Philipp Fischer, and Thomas Brox. U-net: Convolutional networks for biomedical image segmentation. In *International Conference on Medical image computing and computer-assisted intervention*, pages 234–241. Springer, 2015.
11. Patrice Y Simard, David Steinkraus, John C Platt, et al. Best practices for convolutional neural networks applied to visual document analysis. In *Icdar*, volume 3, 2003.
12. Chunliang Wang, Bryan Connolly, Pedro Filipe de Oliveira Lopes, Alejandro F Frangi, and Örjan Smedby. Pelvis segmentation using multi-pass u-net and iterative shape estimation. In *International Workshop on Computational Methods and Clinical Applications in Musculoskeletal Imaging*, pages 49–57. Springer, 2018.
13. Alexander D Weston, Panagiotis Korfiatis, Kenneth A Philbrick, Gian Marco Conte, Petro Kostandy, Thomas Sakinis, Atefeh Zeinoddini, Arunjit Boonrod, Michael Moynagh, Naoki Takahashi, et al. Complete abdomen and pelvis segmentation using u-net variant architecture. *Medical physics*, 47(11):5609–5618, 2020.

Appendix B

A direct geometry processing cartilage generation method for datasets with poor cartilage visibility

The following chapter presents the article:

Faezeh Moshfeghifar, Max Kragballe Nielsen, José D. Tascón-Vidarte, Sune Darkner, and Kenny Erleben. “A direct geometry processing cartilage generation method using segmented bone models from datasets with poor cartilage visibility” Computational Biomechanics for Medicine XVI (MICCAI Workshop) 2021.

This work presents our approach to generating subject-specific hip joint cartilage without directly segmenting them from clinical images. We introduce a specialized geometry processing pipeline that uses the bone geometry information around the hip joint and generates the two articular cartilages in the hip joint. These cartilages are subject-specific and have non-uniform thickness across their geometry. Further, our modeling approach guarantees conforming interfaces with their underlying bones and congruent interfaces between the articular interfaces.

These cartilage models were clinically verified, and their anatomical measurements agree with the data reported in the literature. We tested these models in a finite element simulation setup, and the results produced smooth stress distribution with no convergence issues related to the discretized geometry. The research data, including the modeling pipeline, is available on Github (<https://github.com/diku-dk/CarGen>) for public use. The number of available datasets in this work limited our experiments, and we only managed to test this pipeline on ten hip joints. We further tested the compatibility of this approach on other joints, such as the shoulder and the knee joint, but we left further investigation on such joints for future work.

A direct geometry processing cartilage generation method using segmented bone models from datasets with poor cartilage visibility

Faezeh Moshfeghifar¹, Max Kragballe Nielsen¹, José D. Tascón-Vidarte¹, Sune Darkner¹, and Kenny Erleben¹

Department of Computer Science, University of Copenhagen, Denmark.
 {famo,max,jota,darkner,erleben}@di.ku.dk

Abstract. We present a method to generate subject-specific cartilage for the hip joint. Given bone geometry, our approach is agnostic to image modality, creates conforming interfaces, and is well suited for finite element analysis. We demonstrate our method on ten hip joints showing anatomical shape consistency and well-behaved stress patterns. Our method is fast and may assist in large-scale biomechanical population studies of the hip joint when manual segmentation or training data is not feasible.

Keywords: Cartilage Generation · Hip Joint · Finite Element Analysis.

1 Introduction

The femur and pelvic bones come together in the hip joint (HJ), where the femoral head articulates within the acetabulum’s lunate surface. The lunate surface and all of the femoral head, except the fovea pit, are covered by cartilage tissue allowing unhindered motion in the HJ [27]. The stress distribution on these articular surfaces is often analyzed either experimentally [11, 10], using finite element (FE) analysis [2, 24, 14], or discrete element analysis [28, 32, 30]. The analysis results provide valuable information for studying both healthy and dysplastic hips [16, 28, 24, 32, 31]. The accuracy of these results is highly dependant on the HJ geometries.

HJ morphology is segmented directly from computed tomography (CT) [9, 2, 28, 24, 31] and magnetic resonance imaging (MRI) images [6]. CT and MRI scans contain high contrast images of the bones with clearly visible interfaces. However, it is difficult to identify cartilage tissue due to the tight space in HJ [8] or low image resolution [29]. CT arthrography and manual traction enhance the cartilage visibility and increase the joint space at the cost of being an invasive intervention [9, 24].

This work presents a method to generate subject-specific cartilage models where cartilage segmentation is not feasible. Our method uses only the bone geometries coming together at the HJ and reconstructs the articulating cartilage surfaces based on bone curvature measures and distance measures. Our solution

2 F. Moshfeghifar et al.

is fast, is independent of image modality, and preserves anatomical properties compared to previous methods. We validated our method by comparing the anatomical properties to other works, as detailed in section 4 [1, 20, 15, 25]. Additionally we tested their performance in a FE analysis setup. Our goal is to obtain consistent and stable cartilage models for FE analyses. For now, patients with HJ atypical geometries or pathology are out of the scope of this method.

2 Related work

The femur and pelvis can be segmented using manual [2, 24], semi-automatic [9, 28, 18], or fully automated approaches [17, 31, 6].

When cartilage is manually segmented, the thickness and interfaces are either delineated from the images, assigned uniformly, or approximated by a radius representing the smoothed joint space mid-line [2, 28, 24]. This manual process is time-consuming and is limited by the users' clinical expertise and image resolution. Our method ensures conforming surfaces and computes thickness directly from bone locality without any need for clinical expertise.

In semi-automated segmentation approaches, the initial cartilage geometry is delineated automatically, starting from user-defined landmarks. Additional refinement is needed to eliminate rough surfaces, holes, and irrelevant connected tissues [9, 28]. In contrast, our method only relies on bone surfaces and does not need landmarks or refinement.

With the advancements in computational morphometrics, automated cartilage segmentation is possible by combining bone statistical shape models with population-averaged cartilage thickness maps [30] or geometric constraints [6]. Automatic segmentation is a cost-effective approach and reduces the need for pre-processing data [30]. However, segmented data and prior information is needed to train such models. In contrast, our method does not require training data and is agnostic to data-shift problems.

Other approaches simplify the joint to a perfect ball in socket joint and fit the bone-cartilage and cartilage-cartilage interfaces to spheres or rotational conchoids [2, 21, 32]. These simplifications can have an effect on the cartilage contact pressure and contact area [2]. Our work provides non-uniform cartilage thickness while maintaining conforming interfaces.

3 Methodology

The proposed cartilage generation method is based only on bone geometry and distance measures. Thus, the algorithm is sensitive towards the quality of the segmented bone mesh, which we assume has been preprocessed to remove irregularities and segmentation artifacts. We will focus on the hip joint and generate cartilage with respect to either the pelvis or femur, depending on which bone the cartilage attaches to. We will need to generate cartilage twice: once for the femur and once for the pelvis. We define the geometry of each bone as the vertices and faces $(\mathcal{V}, \mathcal{F})$ of a triangle mesh, where $\mathcal{V} \in \mathbb{R}^{N \times 3}$ and $\mathcal{F} \in \mathbb{Z}_{0+}^{K \times 3}$ for

a mesh consisting of N vertices and K faces. We refer to the bone where cartilage attaches as the *primary bone*, $(\mathcal{V}_P, \mathcal{F}_P)$, and the other bone as the *secondary bone*, $(\mathcal{V}_S, \mathcal{F}_S)$. The generated cartilage will be a triangle surface mesh $(\mathcal{V}_C, \mathcal{F}_C)$. Our method can be summarized as the steps:

Distance Filtering: Select an initial subset of the primary bone as the *bone-attached* cartilage region based on the distance to the secondary bone;

Curvature-Based Region Filling: Apply our curvature-based region filling approach to ensure the bone-attached cartilage region extends to anatomical lines;

Extrusion: Extrude a subset of the bone-attached region towards the secondary bone;

Harmonic Boundary Blending: Interpolate between the boundary of the extruded and bone-attached regions to create a soft blend.

3.1 Distance Filtering

For now, we will focus on the femoral side of the hip joint and describe the femur as the primary bone and the pelvis as the secondary. We select faces on the primary bone, which will serve as an initial guess of the bone-attached cartilage region. We base our choice on the distance between the face barycenters of the primary bone and the secondary bone vertices. That is, provided the distance parameter, δ , we construct the set of faces,

$$\{\mathbf{f} \in \mathcal{F}_P : \min_{\mathbf{v} \in \mathcal{V}_S} \|\mathbf{BC}(\mathbf{f}) - \mathbf{v}\| \leq \delta\} \quad (1)$$

where $\mathbf{BC}(\mathbf{f})$ is the barycenter of face \mathbf{f} . We refer to this subset of faces and vertices as \mathcal{F}_C^D and its corresponding vertices as \mathcal{V}_C^D . The distance filter parameter, δ , should be based on the gap between the femur and pelvis, as it determines the initial approximation quality. The femur’s initial estimate must be located above the anatomical line of the femoral head (Fig. 1a). Otherwise, we do not enforce any restrictions on δ . To provide additional robustness to the initial guess, we trim the outer boundary by removing layers from its outer rim and discarding faces with two boundary edges. The trimming helps ensure the initial estimate does not become too large, and in particular, makes it simpler to avoid selecting triangles crossing the natural ridges of the bone.

The pelvis is more sensitive to the distance filtering parameter than the femur, as most of the cartilage exists in a plateau in the pelvic socket. This implies the bone-attached region does not require any additional refining, as the initial estimate accurately aligns with anatomical lines (Fig. 1d). The distance filtering step typically results in fragmented bone-attached regions, and before we proceed, we discard all but the largest of these regions (Fig. 1f). We can safely discard the smaller regions, as we grow the cartilage during the next step of our algorithm to incorporate all triangles within an area of similar curvature.

4 F. Moshfeghifar et al.

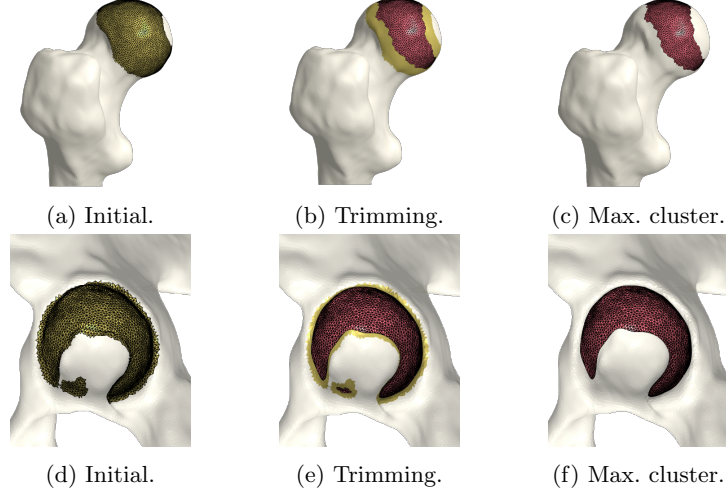


Fig. 1: Computing initial bone-cartilage interface for femur ((a)-(c)) and pelvis ((d)-(f)). Initially, in (a) and (d), triangles on the surface of the femur and pelvis are selected based on the distance to the opposite bone (Eq. (1)). Afterwards, in (b) and (e), the initial sets are trimmed to remove triangles that only have one neighbour. The trimmed region can be seen in red on top of the initial guess in yellow. Finally, we select the biggest cluster of triangles as our initial estimate of the bone-attached region for both femur and pelvis ((c) and (f)).

3.2 Curvature-Based Region Filling

The initial estimate of the bone-side femoral cartilage does not yet fully cover the cartilage zone on the femoral head (Fig. 1c). The femoral cartilage border is observed as a change in the curvature between the femoral head and the neck. In this work, the principal curvatures, κ_{\min} and κ_{\max} , are computed by fitting local frames to a neighborhood around each vertex [23]. This method approximates the Laplace-Beltrami operator in the immediate neighbourhood of each vertex to save computation time. The neighborhood size, \mathcal{N} , can be used as a scaling factor to control how many smaller variations to include in the curvature estimation (Fig 2), and when \mathcal{N} is sufficiently large we will arrive at the same curvatures as can be computed using the mesh laplacian.

Denoting the boundary of \mathcal{F}_C^D as Γ_C^D , we grow the cartilage such that,

$$\mathcal{F}_C^D \leftarrow \mathcal{F}_C^D \cup \{\mathbf{f} \in \Gamma_C^D : \kappa_1 \leq \kappa_{\mathbf{f}} \leq \kappa_2\} \quad (2)$$

where κ_1 and κ_2 denote the minimal and maximal curvature of the region at the femoral head and $\kappa_{\mathbf{f}}$ is the curvature of face \mathbf{f} . We grow the cartilage iteratively using Equation (2) until the region contains all faces in \mathcal{F}_C^D (Fig. 2d).

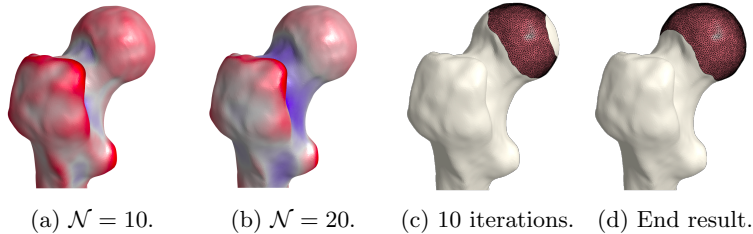


Fig. 2: **(a)-(b)** The effect of changing the neighborhood size, \mathcal{N} , in terms of mean curvature. Red regions correspond to positive curvature directions, while blue regions correspond to negative directions. Note that smaller variations in the surface geometry influence the curvature measure less as the neighborhood size increases. **(c)-(d)** Observe in Fig 1c the initial estimate of the bone-attached region, in **(c)** the bone-attached region after 10 iterations of Equation (2), and in **(d)** the final result, when no more faces satisfy Equation (2).

3.3 Extrusion

As this is a trait of healthy cartilage, we expect the generated geometry to have a high degree of congruence. We extrude vertices based on the minimal distances between the bones and choose the midpoint as the extrusion height to guarantee congruence. This approach ensures the conformity of the cartilage-cartilage interface. We want the shape to thin out as we get further away from the contact center to mimic the real cartilage shape. The faces to extrude, are chosen to be a copy of the bone-attached estimate, $(\mathcal{V}_C^D, \mathcal{F}_C^D)$, and are denoted by $(\mathcal{V}_C^E, \mathcal{F}_C^E)$: the extruded geometry. We assign height to each vertex in the extrusion region, $\mathbf{v} \in \mathcal{V}_C^E$, based on the smallest distance to the second bone as,

$$\mathbf{v} \leftarrow \mathbf{v} + \frac{1}{2} \mathbf{n} \min_{\mathbf{v}_S \in \mathcal{V}_S} \|\mathbf{v} - \mathbf{v}_S\|_2 \quad (3)$$

where \mathbf{n} is the unit outward normal direction of vertex \mathbf{v} . For the pelvis, the faces we extrude are a copy of the bone-attached region. As the pelvic bone-attached region does not need growing, we shrink the set of faces to be extruded by applying the same trimming approach as described in Section 3.1. We then extrude the reduced set of faces (Equation (3)), using the distances from the pelvis to the femur.

3.4 Harmonic Boundary Blending

The final step of the cartilage generation is to connect the bone-attached region, $(\mathcal{V}_C^D, \mathcal{F}_C^D)$, and the extruded surface, $(\mathcal{V}_C^E, \mathcal{F}_C^E)$. Referring back to Section 3.3 we know that $\mathcal{F}_C^E \subset \mathcal{F}_C^D$. We create a copy of the set $\mathcal{F}_C^D \setminus \mathcal{F}_C^E$ and denote it as \mathcal{F}_C^H . This new set will connect the bone-attached region to the extruded surface and consists of the faces from the bone-attached region not initially selected

6 F. Moshfeghifar et al.

for extrusion. To create a smooth blend between the disjoint surfaces, we apply a *biharmonic weighting* scheme. We compute the blended extrusion thickness between the two regions by minimizing the Laplacian energy on the boundary of the domain, Γ . The extrusion thickness is then the minimizers of,

$$\arg \min_{\mathbf{w}} \sum_{w_j \in \mathbf{w}} \frac{1}{2} \int_{\Gamma} \|\Delta w_j\|^2 dV \quad (4)$$

subject to constraints enforcing interpolation between the boundary of the bone-attached region and the boundary of the extruded region. The Laplacian energy is discretized using the FEM method and subsequently solved using an active set method [22]. For more details, we refer the reader to [12]. The resulting displacements \mathbf{w} are then applied to the vertices of \mathcal{V}_C^H as,

$$\mathbf{v}_j \leftarrow \mathbf{v}_j + \mathbf{n}_j w_j, \quad \forall \mathbf{v}_j \in \mathcal{V}_C^H. \quad (5)$$

That is, we extrude each vertex \mathbf{v}_j in the direction of its normal by the displacement w_j . As a final step, we invert the bone-attached face normals before collecting the three disjoint sets of faces and vertices into a single mesh, $(\mathcal{V}_C, \mathcal{F}_C)$. Observe in Fig. 3 the cartilage sub-surfaces combined into a single mesh.

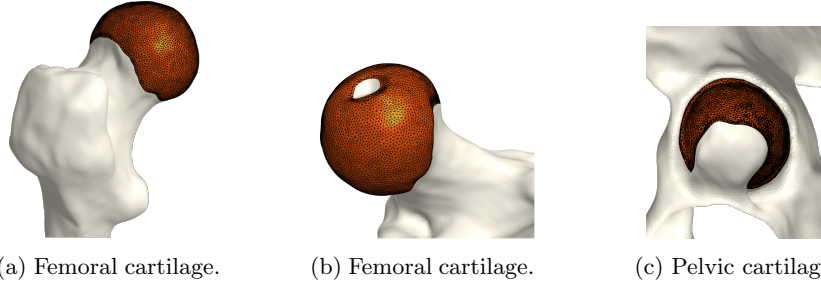


Fig. 3: The final cartilage generated by our method for a femur (a), (b) and a pelvis (c). Notice how the cartilage aligns with the anatomical lines.

4 Results

We use five CT scans from the TCGA-BLCA collection publicly available at the Cancer Imaging Archive [3]. These subjects are in a supine position and have no diagnosed disease related to the HJ. Each dataset contains a left and right HJ summing up to ten HJs. We generate pelvic and femoral cartilages for all ten joints.

Our algorithm is implemented in Python using the Libigl library [13]. To quantify the speed of our method, we timed the generation of femoral and pelvic

cartilages for all ten joints. All cartilages are generated on a MacBook Pro 2018 with a 2.7 GHz quad-core Intel i7. The initial bone geometries for the ten HJs consist of a similar number of triangles (65k triangles on average). We include all steps described in Section 3 in the computation time and exclude the time needed for segmentation and preprocessing of the bone models. We observe that, on average, femoral cartilage reconstruction takes 39.90s and pelvic cartilage reconstruction takes 12.82s. These results show that the time needed to construct the femoral cartilage is significantly higher than for the pelvic cartilages - a factor of three times higher. The femoral cartilage is the only cartilage where the initially trimmed layer (shown in Figure 1b) needs to be grown, explaining the difference in time. It should be noted that while generating a single piece of cartilage takes less than a minute, generating a *good* model of the cartilage takes significantly longer. The time needed to generate such cartilage model includes the time required to calibrate the free parameters of our model. In our experience, the parameters for one patient generally translate well to other models, which means that only minimal tuning is required once a good set of parameter values have been found for a single patient. See supplementary material for the parameters used to generate the cartilage models.

We have qualitatively verified that the articulating surfaces in all the ten HJs are detected correctly regardless of their anatomical variance using visual inspection of overlays as shown in Fig. 4. As desired, we observe a high degree of congruence between the opposing joint surfaces, meaning no gaps or overlaps in the cartilage-cartilage interface. Moreover, we observe a smooth transition towards the bone geometries as expected from the correct anatomy. The parameter values used to generate the cartilage from Fig. 5a. The free parameters are the neighbourhood-size used to estimate the curvature of the bone (\mathcal{N}); the minimum and maximum curvature in the cartilage region ($\kappa_{\min}, \kappa_{\max}$; Eq. (2)); the distance parameter in *mm* (δ ; Eq. 1); and the number of times the outer boundary should be trimmed (N_{trim}). Here, the curvature based parameters ($\mathcal{N}, \kappa_{\min}, \kappa_{\max}$) are only used for the femur. See supplementary material for more visual comparisons.

Further, we quantitatively compare values of our cartilage’s geometric measures to data obtained from the literature to assess that we agree with state-of-the-art reported values. Results are in Table 1. We observe that our method agrees with the range of values from both manual and semi-automated approaches [1, 20, 15, 25].

Next, we analyze the simulation quality of the generated models in an FE analysis setup. We use the Tetgen package to generate a volumetric mesh with tetrahedral elements for each geometry[26]. Using a displacement-controlled simulation in the FEBio software package [19], we push the pelvis on top of the femur, representing a pseudo stance position. Considering the stance position, the distal femur is fixed in the x,y, and z-directions. The pelvis is moved in the z-direction by *1mm* towards the femur. We simplified the mechanical behavior of all the tissues to isotropic and linearly elastic. The material properties are based on the review in [29]. The bone-cartilage interfaces are modeled as *Tied*

8 F. Moshfeghifar et al.

Table 1: Geometric measure comparison between our method and literature

Measure	Study	# of hip joints	Femur	Pelvis
Mean thickness (mm)	Our	10	0.81 ± 0.08	1.05 ± 0.06
	[1]	1	1.5 ± 0.5	1.6 ± 0.4
	[20]	26	1.18 ± 0.06	1.26 ± 0.04
	[15]	11	1.0	1.8
	[25]	23	-	3.5 ± 0.9
	[2]	-	1.28	1.28
Bone coverage area(mm^2)	Our	10	5349.41 ± 660.51	2848.98 ± 351.86
	[25]	23	-	1634 ± 400
Bone coverage percentage	Our	10	-	$39\% \pm 7$
	[7]	16	-	34%
Contact area (mm^2)	Our	10		1732.01 ± 281.06

contacts. An augmented surface contact algorithm with friction-less tangential interaction is applied to the cartilage-cartilage interfaces allowing unhindered motion in the HJ.

Fig. 4 visualizes the von Mises stress pattern on the pelvic cartilage for one HJ. More are shown in the supplementary material. We have verified that no spurious stress peaks appear and that stress values change gradually and smoothly across the cartilage. Further, the high-stress areas are located in the up-direction, as we expect from the applied displacements. The stress values and patterns are not to be confused with those from a real stance. They only serve as a verification test of simulation properties. For such a simulation, we require ligaments and muscles to stabilize the girdle and a correction from sublime pose bias.

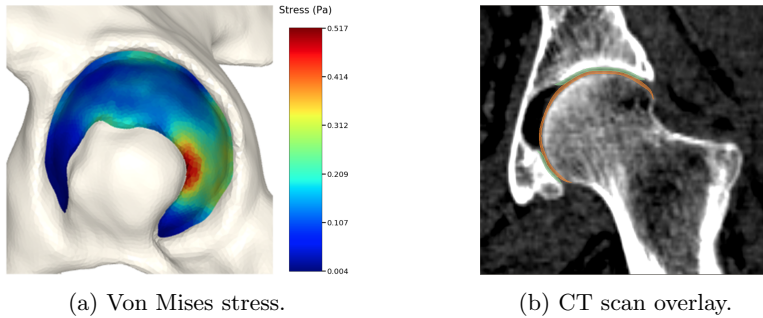


Fig. 4: The von Mises stress patterns ((a)) and the generated cartilage imposed on the CT scan from which the bone was extracted ((b)). Notice the high level of congruence in the cartilage-bone interfaces and cartilage-cartilage interface.

5 Discussion and Conclusion

The results show our method produces similar cartilage to manual segmentation and adheres to our clinical assumptions about cartilage morphology [27]. The high congruence level prevents potential spikes and peak stresses in the articulating surfaces, resulting in continuous stress distribution in the HJ.

Our subjects are in a supine position, which means the cartilage is under a horizontal load. In this case, the bones are not in an unloaded position, causing the generated cartilages to be in a pre-load state. The supine position explains the difference between the cartilage thickness and contact area compared to other studies. One solution is to relocate the bone geometries to the desired position before generating the cartilages or optimizing the rest shape used in the FE analysis. Moreover, as we measure the contact area before running any simulations, our results differ from other studies reporting this value as a simulation result in different gait cycles.

As we rely on the bone curvatures for cartilage-bone interface definition, accurate bone geometries are crucial for realistic results. If the segmented bones are too smooth or coarse, the final product will not agree with real cartilage anatomy. We want to investigate further detailed geometric validation of our method; however, no public databases contain segmented cartilage for hip joints to the best of our knowledge. We leave this for future work.

The FE analysis results show that the generated models produce smooth stress patterns in a pseudo stance without any geometry-related convergence issues. As mentioned in section 4, these results only serve as a verification test of simulation properties. We need a more advanced simulation setting to model a real stance position. We leave this for future work. Moreover, we believe that minor modifications will estimate the shoulder joint cartilage since it has a similar ball-in-socket structure. Fig. 5 shows early evidence of generalization. In contrast, other joints, such as the knee joint, are challenging. We leave other joint types for future work.

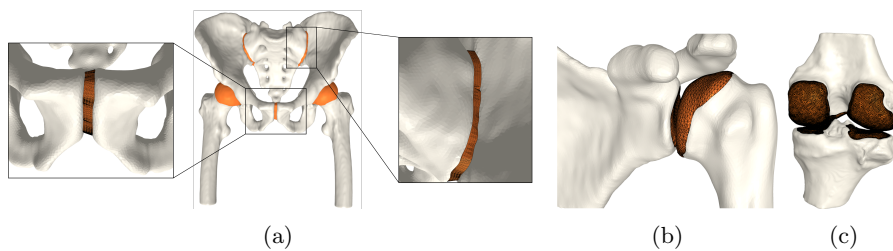


Fig. 5: **a)** All generated cartilages. Zoom boxes highlight the pubic and sacroiliac joint cartilages. **b)** Shoulder joint cartilage **c)** Femoral and tibial cartilage in the knee joint. Bone models are acquired from available datasets [3, 5, 4].

10 F. Moshfeghifar et al.

In conclusion, we have created a method to automate the reconstruction of healthy subject-specific HJ cartilages independent from clinical images. The proposed method is fast and preserves the anatomical properties of the cartilage tissue. The proposed method generates high-quality cartilage without the need for any manual segmentation or training data. We have shown the cartilage models can be used in FE analysis and believe our method will enable large-scale population studies. Future work will extend the geometric principles to abnormal HJs and other joints such as the shoulder and knee joint. Our code is open-source and available from <https://github.com/diku-dk/CarGen>.

6 Acknowledgments

This project has received funding from the European Union's Horizon 2020 research and innovation programme under the Marie Skłodowska-Curie grant agreement No. 764644. This paper only contains the author's views, and the Research Executive Agency and the Commission are not responsible for any use that may be made of the information it contains.

This project has also received funding from Independent Research Fund Denmark (DFF) under agreement No. 9131-00085B.

References

1. Anderson, A.E., Ellis, B.J., Maas, S.A., Peters, C.L., Weiss, J.A.: Validation of finite element predictions of cartilage contact pressure in the human hip joint. *Journal of biomechanical engineering* **130**(5) (2008)
2. Anderson, A.E., Ellis, B.J., Maas, S.A., Weiss, J.A.: Effects of idealized joint geometry on finite element predictions of cartilage contact stresses in the hip. *Journal of biomechanics* **43**(7), 1351–1357 (2010)
3. Clark, K., Vendt, B., Smith, K., Freymann, J., Kirby, J., Koppel, P., Moore, S., Phillips, S., Maffitt, D., Pringle, M., et al.: The cancer imaging archive (tcia): maintaining and operating a public information repository. *Journal of digital imaging* **26**(6), 1045–1057 (2013)
4. Dzialo, C.M., Pedersen, P.H., Jensen, K.K., de Zee, M., Andersen, M.S.: Evaluation of predicted patellofemoral joint kinematics with a moving-axis joint model. *Medical engineering & physics* **73**, 85–91 (2019)
5. Dzialo, C., Pedersen, P., Simonsen, C., Jensen, K., de Zee, M., Andersen, M.: Development and validation of a subject-specific moving-axis tibiofemoral joint model using mri and eos imaging during a quasi-static lunge. *Journal of biomechanics* **72**, 71–80 (2018)
6. Gilles, B., Magnenat-Thalmann, N.: Musculoskeletal mri segmentation using multi-resolution simplex meshes with medial representations. *Medical image analysis* **14**(3), 291–302 (2010)
7. Harris, M.D., Anderson, A.E., Henak, C.R., Ellis, B.J., Peters, C.L., Weiss, J.A.: Finite element prediction of cartilage contact stresses in normal human hips. *Journal of Orthopaedic Research* **30**(7), 1133–1139 (2012)
8. Henak, C.R., Anderson, A.E., Weiss, J.A.: Subject-specific analysis of joint contact mechanics: application to the study of osteoarthritis and surgical planning. *Journal of biomechanical engineering* **135**(2) (2013)

9. Henak, C.R., Carruth, E.D., Anderson, A.E., Harris, M.D., Ellis, B.J., Peters, C.L., Weiss, J.A.: Finite element predictions of cartilage contact mechanics in hips with retroverted acetabula. *Osteoarthritis and cartilage* **21**(10), 1522–1529 (2013)
10. Ipavec, M., Brand, R., Pedersen, D., Mavčič, B., Kralj-Iglič, V., Iglič, A.: Mathematical modelling of stress in the hip during gait. *Journal of Biomechanics* **32**(11), 1229–1235 (1999)
11. Ipavec, M., Iglič, A., Iglič, V.K., Srakar, F.: Stress distribution on the hip joint articular surface during gait. *Pflügers Archiv* **431**(6), R275–R276 (1996)
12. Jacobson, A., Baran, I., Popovic, J., Sorkine, O.: Bounded biharmonic weights for real-time deformation. *ACM Trans. Graph.* **30**(4), 78 (2011)
13. Jacobson, A., Panozzo, D., et al.: libigl: A simple C++ geometry processing library (2018), <https://libigl.github.io/>
14. Jorge, J., Simões, F., Pires, E., Rego, P., Tavares, D., Lopes, D., Gaspar, A.: Finite element simulations of a hip joint with femoroacetabular impingement. *Computer methods in biomechanics and biomedical engineering* **17**(11), 1275–1284 (2014)
15. Lazik, A., Theysohn, J.M., Geis, C., Johst, S., Ladd, M.E., Quick, H.H., Kraff, O.: 7 tesla quantitative hip mri: T1, t2 and t2* mapping of hip cartilage in healthy volunteers. *European radiology* **26**(5), 1245–1253 (2016)
16. Li, F., Chen, H., Mawatari, T., Iwamoto, Y., Jiang, F., Chen, X.: Influence of modeling methods for cartilage layer on simulation of periacetabular osteotomy using finite element contact analysis. *Journal of Mechanics in Medicine and Biology* **18**(02), 1850018 (2018)
17. Lindner, C., Thiagarajah, S., Wilkinson, J.M., Wallis, G.A., Cootes, T.F., arcO-GEN Consortium, et al.: Accurate bone segmentation in 2d radiographs using fully automatic shape model matching based on regression-voting. In: *International Conference on Medical Image Computing and Computer-Assisted Intervention*. pp. 181–189. Springer (2013)
18. Lopes, D.S., Pires, S.M., Barata, C.D., Mascarenhas, V.V., Jorge, J.A.: The hip joint as an egg shape: a comprehensive study of femoral and acetabular morphologies. *Computer Methods in Biomechanics and Biomedical Engineering: Imaging & Visualization* **8**(4), 411–425 (2020)
19. Maas, S.A., Ellis, B.J., Ateshian, G.A., Weiss, J.A.: Febio: finite elements for biomechanics. *Journal of biomechanical engineering* **134**(1), 011005 (2012)
20. Mechlenburg, I., Nyengaard, J.R., Gelineck, J., Soballe, K.: Cartilage thickness in the hip joint measured by mri and stereology—a methodological study. *Osteoarthritis and cartilage* **15**(4), 366–371 (2007)
21. Menschik, F.: The hip joint as a conchoid shape. *Journal of Biomechanics* **30**(9), 971–973 (1997)
22. Nocedal, J., Wright, S.: *Numerical optimization*. Springer Science & Business Media (2006)
23. Panozzo, D., Puppo, E., Rocca, L.: Efficient multi-scale curvature and crease estimation. *Proceedings of Computer Graphics, Computer Vision and Mathematics (Brno, Czech Republic)* **1**(6) (2010)
24. Russell, M.E., Shivanna, K.H., Grosland, N.M., Pedersen, D.R.: Cartilage contact pressure elevations in dysplastic hips: a chronic overload model. *Journal of orthopaedic surgery and research* **1**(1), 6 (2006)
25. Schmaranzer, F., Helfenstein, R., Zeng, G., Lerch, T.D., Novais, E.N., Wylie, J.D., Kim, Y.J., Siebenrock, K.A., Tannast, M., Zheng, G.: Automatic mri-based three-dimensional models of hip cartilage provide improved morphologic and biochemical analysis. *Clinical orthopaedics and related research* **477**(5), 1036 (2019)

12 F. Moshfeghifar et al.

26. Si, H.: Tetgen, a delaunay-based quality tetrahedral mesh generator. *ACM Trans. Math. Softw.* **41**(2), 11:1–11:36 (feb 2015)
27. Standring, S.: *Gray’s anatomy e-book: the anatomical basis of clinical practice*. Elsevier (2020)
28. Tsumura, H., Kaku, N., Ikeda, S., Torisu, T.: A computer simulation of rotational acetabular osteotomy for dysplastic hip joint: does the optimal transposition of the acetabular fragment exist? *Journal of Orthopaedic Science* **10**(2), 145–151 (2005)
29. Vafaeian, B., Zonoobi, D., Mabee, M., Hareendranathan, A., El-Rich, M., Adeeb, S., Jaremko, J.: Finite element analysis of mechanical behavior of human dysplastic hip joints: a systematic review. *Osteoarthritis and cartilage* **25**(4), 438–447 (2017)
30. Van Houcke, J., Audenaert, E.A., Atkins, P.R., Anderson, A.E.: A combined geometric morphometric and discrete element modeling approach for hip cartilage contact mechanics. *Frontiers in Bioengineering and Biotechnology* **8** (2020)
31. Yokota, F., Okada, T., Takao, M., Sugano, N., Tada, Y., Tomiyama, N., Sato, Y.: Automated ct segmentation of diseased hip using hierarchical and conditional statistical shape models. In: *International Conference on Medical Image Computing and Computer-Assisted Intervention*. pp. 190–197. Springer (2013)
32. Yoshida, H., Faust, A., Wilckens, J., Kitagawa, M., Fetto, J., Chao, E.Y.S.: Three-dimensional dynamic hip contact area and pressure distribution during activities of daily living. *Journal of biomechanics* **39**(11), 1996–2004 (2006)

Supplementary Material

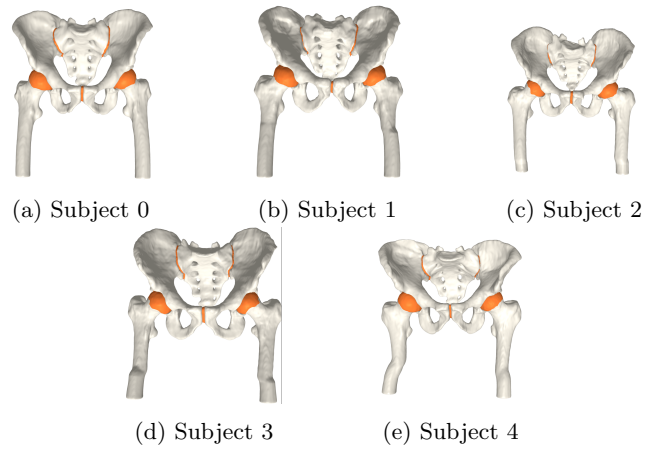


Fig. 1: Cartilage generated for the five subjects in our test set.

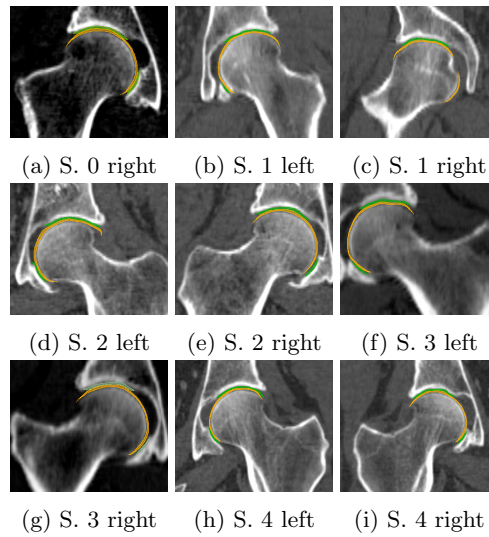


Fig. 2: CT scans overlaid with cartilage and bones for the remaining subjects.

2 F. Moshfeghifar et al.

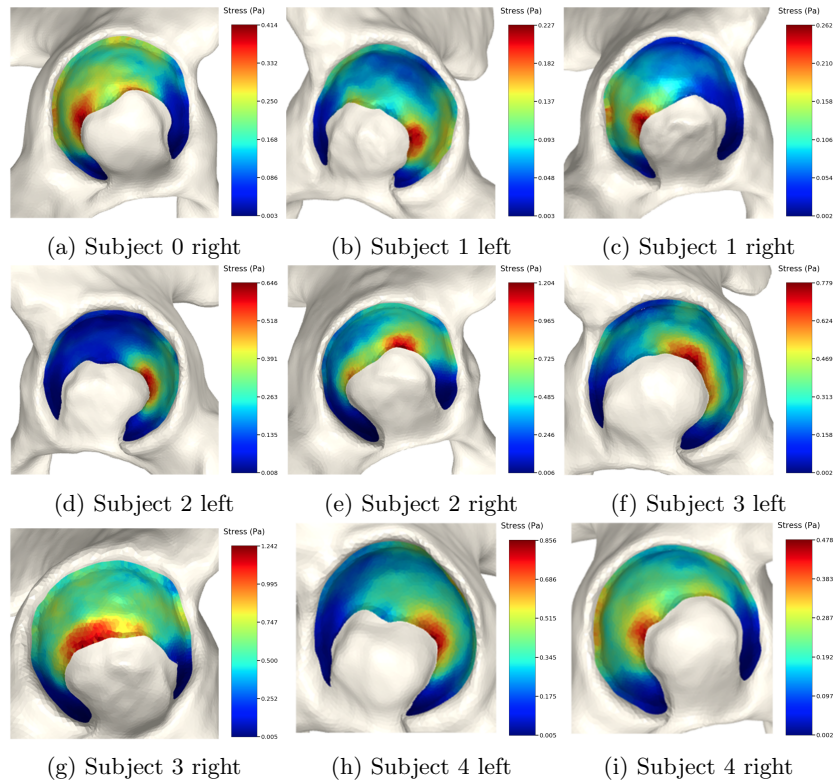


Fig. 3: Von Mises stress patterns on the pelvic cartilage of the right side of the subject shown in Fig. 4 (top left) and the remaining four subjects. We show the left and right pelvic-side cartilage during a simulation identical to the one described in Section 4 of the main paper for each subject.

Parameter	\mathcal{N}	κ_{\min}	κ_{\max}	δ	N_{trim}
Cartilage					
Femoral cartilage	20	0.026	Inf	4.2	7
Pelvic cartilage	-	-	-	3	2
Sacroiliac	-	-	-	4.6	0
Pubic	-	-	-	6	1

Table 2: The parameter values used to generate the cartilage from Fig. 5a. The free parameters are the neighbourhood-size used to estimate the curvature of the bone (\mathcal{N}); the minimum and maximum curvature in the cartilage region ($\kappa_{\min}, \kappa_{\max}$; Eq. (2)); the distance parameter in mm (δ ; Eq. 1); and the number of times the outer boundary should be trimmed (N_{trim}). Here, the curvature based parameters ($\mathcal{N}, \kappa_{\min}, \kappa_{\max}$) are only used for the femur.

Finite Element Analysis Details

The bone geometries are discretized using triangle meshes. The pelvic and femoral cartilages inherit the same triangle size of their corresponding bones. These values are chosen for the “master” and “slave” domains in the HJ contacting zones to ensure coarser meshes on the pelvis side. We generate 4-node tetrahedral quality volume meshes using the Tetgen package [26]. The resulting files are exported as VTK-files to the FEBio solver package [19]. FEBio is an open-source non-linear finite element solver which is widely used in biomechanical applications.

We care about observing smooth stress transitions in the cartilage-cartilage interfaces. Hence, for our validation purpose it suffices that the mechanical behavior of all the tissues are set to be homogeneous isotropic linear-elastic material. The material properties are based on the review in [29]. The Young’s modulus and Poisson’s ratio is 17GPa and 0.3 for bones and 12MPa and 0.45 for the cartilages. The bone-cartilage interfaces are modeled as *Tied facet-on-facet* type of contact in FEBio. A *Sliding facet-on-facet* type of contact is applied to the cartilage-cartilage interface. This is solved as an augmented Lagrangian model with friction-less tangential interaction allowing unhindered motion in the HJ.

The HJ behavior is analyzed under a quasi-static loading condition. Therefore, the pelvis and the femur is expected to be in an equilibrium state. We use a displacement-controlled simulation where we push the pelvis on top of the femur, representing a pseudo stance position. We prescribe the nodal displacement field and the load will be given implicitly during the simulation. Considering the stance position, the distal femur is fixed in the x, y, and z-directions. The pelvis is moved in the z-direction towards the femur.

Appendix C

LibHip: An Open-Access Hip Joint Model Repository suitable for Finite Element Method Simulation

The following chapter presents the article:

Faezeh Moshfeghifar, Torkan Gholamalizadeh, Zachary Ferguson, Teseo Schneider, Michael Bachmann Nielsen, Daniele Panozzo, Sune Darkner, Kenny Erleben. “LibHip: An Open-Access Hip Joint Model Repository suitable for Finite Element Method Simulation” Under review at Journal of Computer Methods and Programs in Biomedicine. 2022

This work aimed to provide a model repository of multiple subject-specific hip joint finite element models. We further proposed a novel workflow to generate these models with minimal user interaction, using cutting-edge geometry processing tools from the field of computer science. Our work is one of the largest model repositories concerning the number of subjects and regions of interest in the hip joint area.

The anatomical representations in our work cover the bones and cartilages in the hip joint area. The cartilage modeling pipeline is a continuation of our work in Appendix B which is improved and extended to the pubic symphysis and the sacroiliac joints. These clinically verified models have high-quality discretization, conforming and congruent shared interfaces, and accurate geometries. The simulations produce smooth stress patterns, and the variance among the subjects demonstrates the effect of inter-subject variability and asymmetry in the predicted results.

Our detailed research data, including the clinical images, the segmentation label maps, the finite element models, and software tools, are openly accessible on <https://diku-dk.github.io/libhip/>. In future work, we aim to add additional structures to our models.

This work highly benefited from the international collaboration with the New York University and the clinical collaboration with the Copenhagen University Hospital, Rigshospitalet.

LibHip: An Open-Access Hip Joint Model Repository suitable for Finite Element Method Simulation

Faezeh Moshfeghifar^{a,*}, Torkan Gholamalizadeh^{a,b}, Zachary Ferguson^c, Teseo Schneider^d,
Michael Bachmann Nielsen^{e,f}, Daniele Panozzo^c, Sune Darkner^a, Kenny Erleben^a

^aDepartment of Computer Science, University of Copenhagen, Copenhagen, 2100, Denmark

^bShape A/S, Copenhagen, 1060, Denmark

^cCourant Institute of Mathematical Sciences, New York University, 60 5th Ave, New York, NY 10011, United States

^dDepartment of Computer Science, University of Victoria, Victoria, BC V8P 5C2, Canada

^eDepartment of Clinical Medicine, University of Copenhagen, Copenhagen, Denmark

^fDepartment of Diagnostic Radiology, Copenhagen University Hospital, Copenhagen, Denmark

Abstract

Background and Objective: Population-based finite element analysis of hip joints allows us to understand the effect of inter-subject variability on simulation results. Developing large subject-specific population models is challenging and requires extensive manual effort. Thus, the anatomical representations are often subjected to simplification, and the bilateral variations are often neglected. The discretized geometries do not guarantee conformity in shared interfaces, leading to complications in setting up simulations. Additionally, these models are not openly accessible, challenging reproducibility. Our work provides multiple subject-specific hip joint finite element models, and a novel semi-automated modeling workflow.

Methods: We reconstruct 11 healthy subject-specific models, including the sacrum, the paired hip bones, the paired proximal femurs, the paired hip joints, the paired sacroiliac joints, and the pubic symphysis. The bones are derived from CT scans, and the cartilages are generated from the bone geometries. We generate the whole complex's volume mesh with conforming interfaces. Our models are evaluated using both mesh quality metrics and simulation experiments.

Results: All models are clinically validated and show high-quality discretization with accurate geometries. The simulations produce smooth stress patterns, and the variance among the subjects demonstrates the effect of inter-subject variability and asymmetry in the predicted results.

Conclusions: Our work is one of the largest model repositories with respect to number of subjects and regions of interest in the hip joint area. Our detailed research data, including the clinical images, the segmentation label maps, the finite element models, and software tools, are openly accessible on GitHub. Our aim is empowering clinical researchers to have free access to verified and reproducible models. As future work, we aim for adding additional structures to our models.

Keywords: Hip joint repository, Population-based finite element analysis, Multi-body meshing

*Corresponding author

Email addresses: famo@di.ku.dk (Faezeh Moshfeghifar), torkan@di.ku.dk (Torkan Gholamalizadeh), zfergus@nyu.edu (Zachary Ferguson), eseo@uvic.ca (Teseo Schneider), michael.bachmann.nielsen@regionh.dk (Michael Bachmann Nielsen), panozzo@nyu.edu (Daniele Panozzo), darkner@di.ku.dk (Sune Darkner), kenny@di.ku.dk (Kenny Erleben)

1. Introduction

The Finite element (FE) method brings hip joint models to life by simulating their behavior under given conditions. This method is a numerical approach to solve partial differential equations by discretizing the hip joint domain into a finite mesh [1]. The approximated solutions can simulate the load transfer across the hip joint, define sliding contact between the articular surfaces, and estimate the stress distribution in this area [2, 3]. Such data help researchers understand the underlying mechanism of healthy hip joints and their mechanical alteration in complex disorders, such as hip dysplasia [3–5]. Hip joint FE models offer various contributions to improving current clinical treatment [6], the design of surgical simulators for virtual training [7], and optimizing hip implants [8–11].

1.1. Problem statement

Despite the advantages of FE analyses, most studies assessing the hip joint behavior are based on models from a single or a few subjects. This approach does not account for the effect of the inter-subject variability and leaves uncertainties regarding the generality in the predicted results [12]. On the other hand, population-based studies are limited by clinical resources and the significant amount of time and manual effort to prepare large-scale hip joint models. The hip joint area exhibits multiple structures in contact, and each structure is typically segmented from clinical images, transformed into surface meshes, and then filled with volume mesh elements: this process is time consuming and usually requires extensive manual work by FE specialists.

A common requirement in generating a volume mesh is an explicit definition of the surface mesh, meaning that the surface has to be closed, non-intersecting, and manifold. While these requirements are necessary for identifying the interior part of the surface mesh, they are usually not satisfied by the quality of the segmentation results, and may require extensive manual post-processing. Further, most FE formulation require volume meshes to share faces on adjacent surfaces in the hip joint area, a property which is challenging to enforce for many volume meshing tools. If this property is not satisfied, additional, and often insurmountable, appear in the contact formulation which might lead to invalid simulation results.

1.2. Contributions

We present a hip joint FE model repository designed for FE simulation studies. We are combining cutting-edge geometry processing algorithms to reduce the amount of user interaction in developing FE models and tackle the shortcomings of conventional methods. Figure 1 summarizes our FE modeling workflow. The significant technical contributions and unique traits of these models are outlined below and illustrated in Figure 2.

- *Open-access data aligned with the FAIR guiding principles [13]:* Our population study includes 11 male subjects with no diagnosed disease related to the hip joint. All the models, including the clinical images, the segmentation label maps, the FE models, together with the algorithms to prepare them, are available to scientists [14]. The vision of this approach is to empower clinical researchers to have easy access to verified and reproducible FE models. A senior consultant radiologist has clinically validated the geometry of all the models. The FE model’s simulation performance is verified by running FE analyses and analyzing the estimated results.

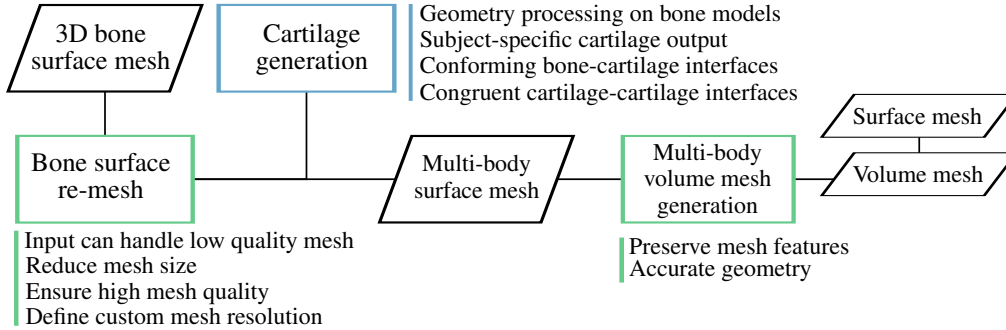


Figure 1: The LibHip modeling flowchart; The workflow is aimed at minimum user interaction and proper FE model features. The blue box presents the shape-related process, and the green boxes indicate discretization-related processes. Our approach starts from the 3D representation of bones and generates the volume and surface mesh of the hip joint area.

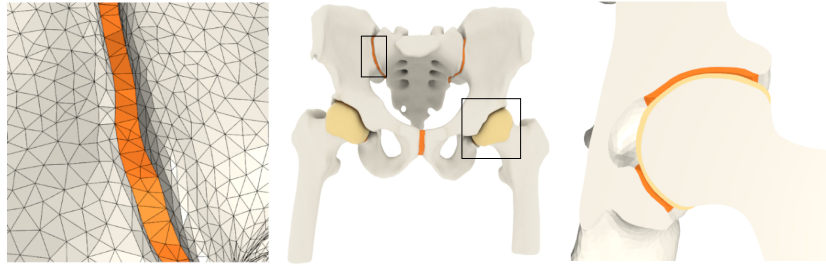


Figure 2: The overview of our modeling features; Middle: The regions of interest covers the sacrum, the paired hip bones, the paired proximal femurs, and all the three joints connecting these bones together; Left: The bone-cartilage interfaces have conforming interfaces. Observe the conforming interfaces between the sacroiliac cartilage and the neighbouring bones; Right: Congruent interfaces between the articular cartilages in the hip joint.

- *A full pelvic girdle with both the hip joints:* All the bones in the hip area encompassing the sacrum, the paired hip bones, and the paired proximal femurs are segmented directly from CT scans. Having all the bone models from both sides of the body preserves bilateral variations and considers the effect of the pelvic girdle in the hip joint behavior.
- *Subject-specific cartilages:* We reconstruct the sacroiliac joints, the pubic symphysis, and the articulating hip joint cartilages semi-automatically and independent of the CT scan data [15]. This approach provides fast, subject-specific cartilages with non-uniform thickness. Modeling cartilage in the inter-bone cavities ensures inter-connectivity of the weight-bearing path in the pelvic girdle. Our joint models maintain conforming boundaries in their bone-attached interfaces. Further, we provide congruent interfaces between the two articular cartilages in the hip joint. The high congruence level prevents potential spikes and peak stresses in the articulating surfaces, resulting in continuous stress distribution.
- *Highly accurate discretization:* We employ a multi-body volume mesh generation that simultaneously generates the whole complex's volume mesh, ensuring neither overlapping nor gaps in the interfaces. This method welds the interface nodes together in the meshing step, avoiding further contact definitions in the simulation setup. We use the Hausdorff distance to measure the geometrical accuracy in our models.

2. Background

Assessing the hip joint behavior through FE analysis requires three main steps: The first is to generate a proper approximation of the anatomical structures; Second, this anatomical information is transformed into surface and volume representations to build a FE model; And lastly, the behavior of this model is studied under a chosen analysis scenario. To gain realistic predictions, we need detailed representations of the hip joint area, including soft and hard tissue, and a flawless discretization to reduce the prediction errors [16].

2.1. Anatomy of the hip joint area

The skeletal structure in the hip joint area is formed by the pelvic girdle reaching the femoral bones in the hip joint. The pelvic girdle consists of the paired hip bones and the sacrum bone in the middle [17]. It serves as a weight-bearing structure, transferring the body weight to the femur through the sacrum bone, the sacroiliac joints, the hip bones, the pubic symphysis, and finally, the hip joints [17]. Posteriorly, the sacrum reaches the hip bones in the sacroiliac joint, and anteriorly, the two hip bones connect at the pubic symphysis. The acetabulum surface of the hip bones articulates within the proximal femur to form the hip joint. The lunate surface of the acetabulum and the femoral head, except the fovea pit, are covered by articular cartilages [17].

2.2. Overview of subject-specific hip joint modeling approaches

Computer-aided design models are simple solutions to capture the overall shape of the hip joint area, e.g., represent the hip joint as a perfect ball-in-socket joint. Even though convenient, such simplifications are shown to overestimate the stress predictions in the hip joint [18, 19]. Subject-specific modeling is another popular choice that solves some of the issues arising from computer-aided design models, thanks to having detailed anatomical information.

The anatomical structures in subject-specific modeling approaches are directly reconstructed based on clinical image modalities such as computed tomography (CT) and magnetic resonance imaging (MRI) [3, 20–22]. CT and MRI scans contain precise bone information; Thus, segmentation using manual [18, 23], semi-automatic [24, 25], or fully automated approaches [26] results in accurate bone geometries.

Further, the subject-specific modeling approach is to account for articulating cartilages. The cartilage thickness and interfaces are often either delineated from the images, assigned uniformly, or approximated by a radius representing the smoothed joint space mid-line [18, 23, 25]. Given the tight space in the hip joint, it is difficult to identify the opposing cartilage interfaces [27]. CT arthrography and manual traction increase the joint space, enhancing cartilage visibility at the cost of being an invasive intervention [23, 24]. In this study, we semi-automatically segment the bone geometries from CT scans and use a fast geometry processing method to create subject-specific cartilages from bone geometries. This method is based on our previous work to create cartilages where cartilage segmentation is not feasible [15].

FE analysis over a *single* hip joint provides valuable information regarding that specific model [20, 22, 28]. However, the hip joint shape and the relative alignment of structures vary among individuals and adding more models in the simulations allow us to account for this variability. It is suggested that there is a significant variation in the hip joint contact mechanics due to the geometrical differences [19, 29]. Currently, a limited number of works use *multiple* hip joint models to study the effect of inter-subject variability, and in most cases, the models are not freely available. Table 1 compares the most related population-based studies to our work.

Table 1: The comparison between some of the most related population-based studies and our work; Most of these works only cover one side of the body and increase the subject numbers by manipulating the existing models. Our work is one of the largest model repositories regarding the number of subject-specific data and the region of interest in the hip joint area.

Study	Subject Data		Modeling style	Body side	Region of interest								Resource availability	
	Healthy	Diseased			HB	PF	SB	HJ	HJ-L	HJ-C	SIJ	PJ		
Harris [29]	CTA/10	-	SS	one	✓	✓	-	✓	✓	-	-	-	I	
Henak [19]	CTA/10	CTA/10	SS	one	✓	✓	-	✓	✓	-	-	-	I	
Zhao [3]	CT/1	3	SS+mirror	both	✓	✓	-	✓	✓	-	-	-	NA	
Chegini [30]	4	4	CAD	one	✓	✓	-	✓	✓	-	-	-	NA	
Russel [31]	1	CTA, X-ray/11	SS+AM	one	✓	✓	-	✓	-	-	-	-	NA	
Liechti [32]	X-ray/1	X-ray/2	CAD	one	✓	✓	-	✓	✓	-	-	-	NA	
LibHip	CT/11	-	SS	both	✓	✓	✓	✓	✓	-	-	✓	✓	I+FEM

CTA: CT arthrography; SS = Subject-specific geometry from images; CAD = Computer Aided Designed models; SS+mirror: half of the model is derived from images and it is flipped to generate the other side; SS+AM: The diseased models are derived from images and the healthy model is generated by deforming the Visible Human Project Model [33]; HB: Hip bone, PS: Proximal femur, Sb: Sacrum bone, HJ: Hip joint, HJ-L: Hip joint labrum, HJ-C: Hip joint capsule, SIJ: Sacroiliac joint, PJ: Pubic joint; I: Availability of the images, FEM: Availability of the Finite Element Models.

Preparing population-based models are challenging: A limited number of models or clinical images of healthy hip joints are available, and the ethical issues regarding radiation exposure prevent custom image acquisition. Unlike Henak and Harris et al., who have performed custom image acquisition on both healthy and pathological subjects [19], most studies only have access to either healthy or diseased images. Thus, they generate more models by post-processing the existing models. For instance, Zhao et al. made multiple diseased models by changing the morphological parameters of a single healthy model [3]. Russel et al. used 11 diseased subjects and built an age-matched healthy hip model by deforming the Visible Human Project model [31, 33]. These approaches fail to provide geometries arising directly from subject-specific images. Our work uses 11 healthy images from The Cancer Imaging Archive. We have chosen open-access images to ensure reproducibility and exterior validity in our method [34].

The region of interest is another challenging issue in population-based modeling. Most modeling approaches do not necessarily include the whole anatomical structures in the hip area. For example, Henak et al. and Harris et al. have chosen to model the hip joint from only one side of the body. The geometry of the rest of the pelvic girdle is ignored, and their effect is presented by boundary conditions [19, 29]. To make bilateral models, Zhao et al. assumed the hip area to be symmetrical along the sagittal plane and flipped the model of one side to generate a symmetrical model [3]. Although these studies provide fundamental predictions of the hip joint behavior, their modeling assumptions are simplified with no consideration of the whole hip area and the bilateral variation, both of which have effects on the hip joint overall behavior. In our work, we show that the hip joint area is not symmetrical, and it is a very invasive assumption to use half of the body in simulations. We quantify the anatomical variation in our models based on well-known anatomical metrics and compare the simulation results of half and bilateral models.

2.3. Surface and volume discretization

The image segmentation label maps are transferred to surface meshes using the marching cube algorithm, and ideally, they should be water-tight two manifold surfaces. Unfortunately, this is rarely the case for clinical data: errors can occur in the segmentation due to insufficient input data, presence of small features, or numerical issues in the contouring methods. Traditionally, these imperfections need to be cleaned up before volumetric meshing, a laborious task, even when using state-of-the-art re-meshing tools [35].

When all surfaces are clean, a volume mesh is created by filling the interior part of each surface. Tetrahedral elements are the most commonly used types of finite elements due to their

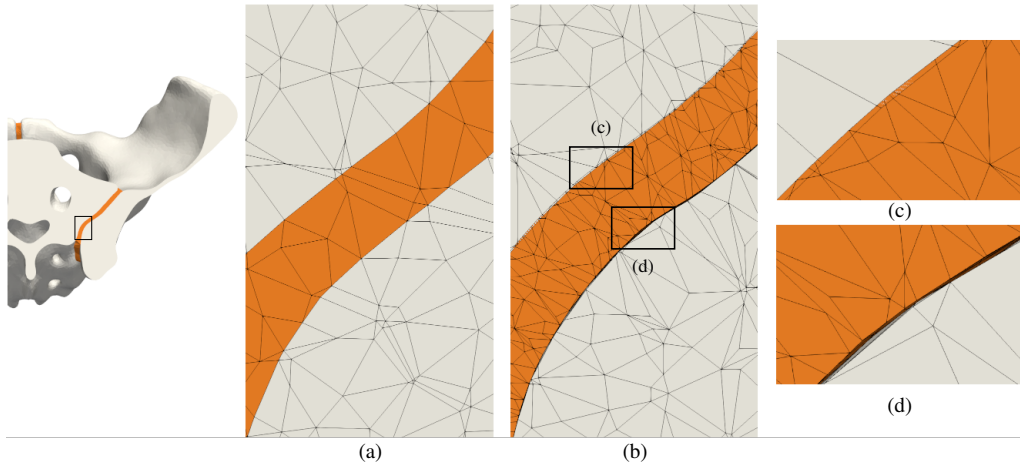


Figure 3: The comparison between *multi-body* and *one-by-one* meshing approaches in the sacroiliac joint; The mesh in (a) is generated using the multi-body meshing approach. This method guarantees conforming interfaces with the hip and sacrum bones. Figure (b) shows the result of the one-by-one mesh generation approach, resulting in overlapping (c) or separated (d) interfaces.

good performance [36] and ease of generation [37, 38]. A variety of approaches, such as Delaunay meshing, advancing front, or grid stuffing are used for volumetric meshing. Due to the high failure rate of these methods [37], the surface cleaning must be iteratively repeated until the meshing algorithm succeeds on all the sub-volumes. Our work adopts a radically different approach to remove this manual and time-consuming step: Using fTetWild [38], we create a single discretization for all surfaces, including their imperfections, and we then extract a consistent volumetric partitioning only after the volumetric meshing is performed. This approach is robust against bad input surface triangles and automatically deals with holes, self-intersections, or inconsistent inside/outside orientation.

Another important property of fTetWild [38] is that the output resolution is decoupled from the input resolution, and it is controlled by an explicit parameter measuring the maximal tolerated geometric error. This is ideal in our setting, as it allows us to generate coarse meshes starting from the fine surface meshes extracted from clinical images. In contrast, traditional approaches have limited control over mesh resolution, as they cannot easily coarsen the surface mesh [39].

Further, conventional volumetric meshing tools mesh the different sub-domains of the hip joint multi-body separately in a one-by-one approach. In contrast, we process all the surfaces of our multi-body model simultaneously, considering them as faces in a single, conforming tetrahedral mesh, and thus allowing them to overlap, have gaps, or other imperfections. We then perform inside/out tests and constructive solid geometry operations as a filtering operation on the resulting tetrahedral mesh, using signed distance as a geometrically robust filter. This approach benefits from naturally guaranteeing conformity between adjacent surfaces in a multi-body model. We refer to [37, 38] for more details on the fTetWild meshing algorithm. Figure 3 compares the one-by-one volume mesh generation versus simultaneous mesh generation.

By *conforming* interface, we mean that the bone-cartilage boundaries have the same discretization in the shared interfaces. If the discretization connectivity differs in the shared interfaces, but the interface shape is still the same, we have a *congruent* interface. Figure 4 illustrates

the conforming and congruent interfaces in the hip joint. The bone-cartilage interfaces conform, while the articular cartilages have congruent interfaces. Conforming interfaces allow us to merge the discretization of the two sub-domains. This is preferred in simulation methods as it reduces the number of variables and the need for adding extra constraints to keep vertices together during simulation. Congruent interfaces in the hip joint allows a smooth load transition between the articular cartilages. Joint congruency evaluates the encasing of the articular cartilages in the hip joint and a way to compare healthy and pathological joints [19].

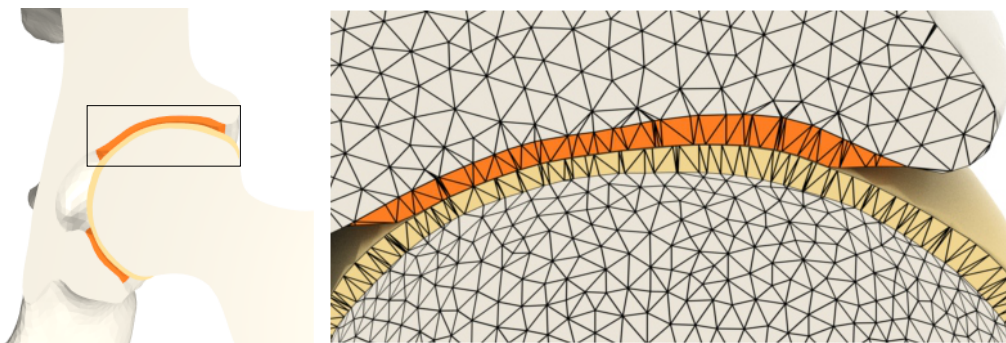


Figure 4: Conforming and congruent interfaces in the hip joint; The cartilages form conforming interfaces with the hip and femoral bone. Notice how each cartilage is sharing the same node with its attached bone. The joint has congruency between the yellow and orange interfaces. These interfaces do not share the same discretization but follow the same curvature. The cross-section wireframe does not represent the true tetrahedrals and is only for visualization purpose.

2.3.1. Finite element method solvers

Various research libraries, commercial codes, and software are available to solve elastic problems with the FE method. However, they are sensitive to user-defined solver settings, unrelated to the physical quantities of interest. For example, contact parameters and the time step size can significantly affect the stability and accuracy of the estimated solutions and even lead to inverted elements. Additionally, in some contact models such as the ones used in Abaqus and FEBio, the user must assign pre-defined contact surfaces. These two surfaces must have specific, and distinct, mesh resolution [40, 41]. FEBio also requires an initial slight penetration between these surfaces to be able to detect the contact surfaces [41].

PolyFEM, in contrast, adopts the Incremental Potential Contact (IPC) formulation [42, 43]. This algorithm requires no manual selection of the contact surfaces and no prescribed mesh resolution. This solver is robust to large deformations and ensures that no elements are inverted using explicit line-search checks [42]. The downside is that it requires an initial configuration free of penetrations (and it preserves this condition throughout the whole simulation [44]). Further, PolyFEM allows adaptive p-refinement on Lagrangian tetrahedral elements, which we use to increase accuracy by employing higher-order basis in thin cartilage layers [45].

In this work, we want to generate models compatible with both strategies. We thus generate two sets of FE models for each subject: With and without a gap between the articular cartilages. We show FE solutions computed using both approaches in Section 4.3.

3. Material and methods

In this section, we explain our modeling workflow, illustrated in Figure 1. We start from the data which we use to reconstruct the anatomical structures. Next, we describe the volume mesh generation step and explain the steps taken to ensure high-quality meshes. Finally, we describe the FE setup that we employ to test the quality of our models.

3.1. Image data

The input to our modeling workflow is the surface mesh of the bony structures. We have chosen to create our input models based on CT scans as this modality is suitable for defining the location and topography of the bones in the hip joint area [46]. We obtain the scans in DICOM format from the open-access Cancer Imaging Archive (CIA) to ensure reproducibility [34].

We select our subjects from the CT Colonography, the Lymph Nodes, and the Cancer Genome Atlas Urothelial Bladder Carcinoma (TCGA-BLCA) collections [47–49]. The scanning procedure in these collections covers the hip joint area explained in Section 2.1. The subjects are in a supine position during the image acquisition, which is the closest to a *unloaded* joint state. We chose 11 subjects with the same gender, age range, with no reported disease related to the hip joint, the most little rotation in the body, high image resolution, and minimum image noise. We further crop the CT scans to the hip joint area to minimize the computational load during segmentation. Next, the cropped images are stored in NIFTI format to store each subject as a single file in our repository while preserving all the essential metadata. Table 2 outlines the image properties and traits for each subject.

Table 2: The specification of image data used to create the input models; All images are selected from the CIA. These images consists of adult male subjects with no reported disease related to the hip joint area. These data are provided to ensure complete transparency in our work.

Model	Sex	Age	CT Scanner	In-plane pixel spacing (mm)	Matrix size (pixels)		CIA Subject ID
					Before crop	After crop	
m1	M	65	GE LightSpeed VCT	[0.85, 0.85, 1.25]	512x512x663	365x221x291	//-AA7M
m2	M	64	GE LightSpeed VCT	[0.78, 0.78, 1.25]	512x512x613	394x215x257	//-AA7O
m3	M	65	Siemens Emotion 6	[0.82, 0.82, 2.5]	512x512x475	378x199x244	//-AA7S
m4	M	56	GE LightSpeed VCT	[0.90, 0.90, 1.25]	512x512x455	362x184x236	//-AA7W
m5	M	73	GE LightSpeed VCT	[0.87, 0.87, 1.25]	512x512x468	389x226x265	//-AA80
m6	M	62	Siemens Emotion 6	[0.69, 0.69, 2.5]	512x512x388	436x256x206	//-AA84
m7	M	51	Siemens Sensation 64	[0.78, 0.78, 1.00]	512x512x520	405x232x250	-4.0004
m8	M	50	-	[0.97, 0.97, -]	512x512x717	399x250x290	*_039
m9	M	60	Siemens Sensation 64	[0.78, 0.78, 1.00]	512x512x617	427x254x318	-4.0002
m10	M	71	Siemens Sensation 16	[0.80, 0.80, 1.00]	512x512x524	400x285x289	-4.0040
m11	M	-	Siemens Sensation 16	[0.82, 0.82, 1.00]	512x512x603	404x230x283	-4.0051

M: male; //:TCGA-4Z; - = 1.3.6.1.4.1.9328.50.4; *:ABD_LYMPH;

3.2. Bone geometry reconstruction

We obtain an explicit surface representation of all the bones using a semi-automated approach implemented in the 3D slicer software package [50, 51]. This method entails initial region labeling, contouring [52], followed by manual refinements to ensure accurate 3D approximations with no rough surfaces, holes, and irrelevant connected tissues.

These bone segmentation are verified by a senior consultant radiologist. The clinical expert initially scrolls through all the segmented slices in each subject and verifies the bone contours and

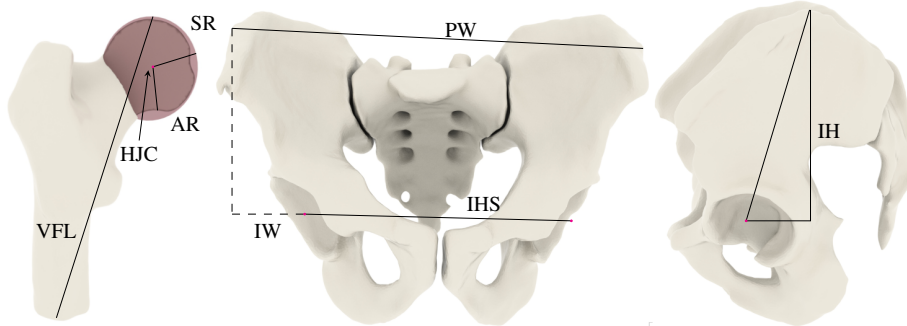


Figure 5: The anatomical measurements of the hip joint area; These parameters quantify the geometry of our models and measure the inter-subject and bilateral variability among subjects. (Left:) A red sphere is fitted to the femoral head. The center of this sphere is the hip joint center (HJC) and the radius (SR) is defined as the simplified femoral head radius. We define the distance between the HJC and the femoral head boundary as the actual femoral head radius (AR). The SR and AR comparison shows the amount of lost subject-specific geometry after simplification. The visible femoral length (VFL) is the most extended visible length in the femur bone. (Middle, Right:) Observe the width of the pelvis (PW), the inter-hip separation (IHS), and the height and width of the ilium (IH, IW).

the existing gaps in the inter-bone cavities. Then, he verifies the anatomical shape and smoothness of the reconstructed 3D surfaces. This procedure justifies the validation of our method in obtaining precise geometries.

3.3. Anatomical measurement

The shape of the hip joint area varies among different subjects and between the two sides of the body. We employ the anatomical measurements of the the bones and cartilages to quantify this variation. Most of the anatomical measurements in literature are based on 2D assessment of the location of measurement [53] or are based on cadaver skeletal measurements [54]. This procedure may not be sufficient for subject-specific 3D geometry analysis [55]. Therefore, we have chosen to obtain the subject-specific anatomical measurements from the 3D surface mesh. These parameters are illustrated in Figure 5.

We fit a sphere to the femoral head and choose the center and radius of this sphere as the *hip joint center (HJC)* and the *simplified femoral head radius (SR)*, respectively. To minimize the bias from manual fitting, we use a least-squares method for spherical fit [56]. We further measure the distance from the HJC to the actual femoral head surface mesh (AR) to see how the geometry of the femoral head deviates from a sphere. We define *The visible femur length (VFL)* as the length of the line connecting the most proximal point of the femur to the mid-point of the most distal part of the same bone; *Width of the pelvis (PW)* is explained as the distance between the most lateral point of the hip bones to the femoral head center; The *Inter-hip separation (IHS)* is assumed as the distance between the paired hip joint centers; The *height of ilium (IH)* is the vertical distance between the most superior part of the hip bones and the hip joint center; The *width of ilium (IW)* is defined by the horizontal distance between the hip joint center and the most lateral point of the hip bones. We compare the left and right HJC, SR, AR, VFL, IH, and IW to capture the bilateral variation w.r.t the sagittal plane.

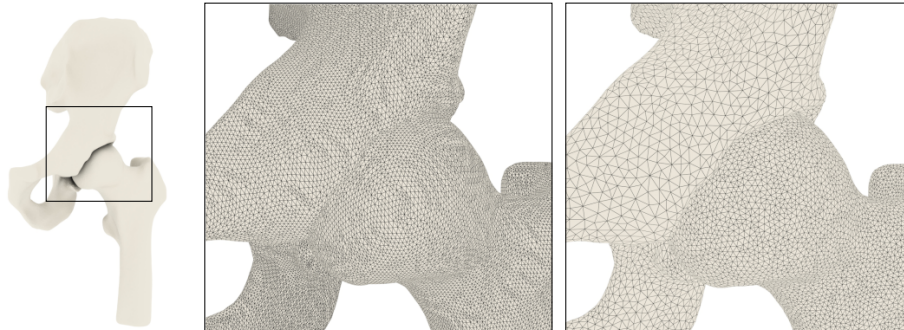


Figure 6: The comparison between the surface mesh output from 3D Slicer and re-meshed surface mesh in fTetWild; The fTetWild result shows a clean mesh with no dense or erroneous triangles. The coarser mesh on the hip side guarantees robust contact definition in the FE analysis.

3.3.1. Bone surface mesh re-meshing

As explained in Section 2.3 and illustrated in Figure 6, the bone surface mesh extracted from the CT scans are typically dense and may have poor quality, and other imperfections. We need to improve the quality and resize the triangles for two particular reasons: 1) Our cartilage generation algorithm in Section 3.4 uses the bone surface mesh to generate the base of the cartilages [15]. Thus, the cartilage’s surface mesh quality depends on the quality of its underlying bone mesh quality; 2) Some FE solvers enforce specific requirements on the mesh resolution for robustly detecting contact points [40, 41].

We use fTetWild to mesh the volume of the surface boundary and re-extract the surface of the volume mesh as the resulting re-meshed surface [37]. This meshing method allows vertices of the boundary of the volumetric mesh to move within an ε envelope of the winding number field level-set that defines the surface geometry [37]. We tune the epsilon (ε) and the edge-length (l) parameters in fTetWild to provide different mesh densities between the articular joints in the hip joint. This guarantees coarser meshes on the acetabular cartilage.

3.4. Cartilage geometry reconstruction

We apply a specialized geometry processing method to generate subject-specific cartilages for the paired hip joints, the paired sacroiliac joints, and the pubic symphysis. This method was initially introduced by Moshfeghifar et al. to generate subject-specific hip joint cartilages independent of image modalities [15]. The cartilage results have conforming interfaces with the underlying bones and have non-uniform thickness across the tissue. Our work adds new ideas to this algorithm to improve the hip joint results and extends this method to the other two joints.

The sacroiliac joint and the pubic symphysis have a limited range of motion to provide stability and strength in the pelvic girdle [17]. We model these joints as *single-piece* cartilages, filling the inter-bone cavity. On the other hand, the hip joint has a higher degree of freedom, allowing free rotation of the femur within the acetabulum cusp. Thus, we model this joint as *double-piece* cartilages attached to the acetabulum and the femoral head.

Each cartilage is generated based on the shape and distance of the involved bones in the joint. The geometry of each bone is defined as $(\mathcal{V}, \mathcal{F})$, where $\mathcal{V} \in \mathbb{R}^{N \times 3}$ is a set of mesh vertices, and $\mathcal{F} \in \mathbb{Z}^{K \times 3}$ is a set of mesh faces; N and K denote the number of vertices and faces, respectively. The cartilage reconstruction starts from one of the bones, referred to as the

primary bone ($\mathcal{V}_P, \mathcal{F}_P$), and grows toward the second bone, referred to as the *the secondary bone* ($\mathcal{V}_S, \mathcal{F}_S$). The steps are summarized below and illustrated in Figure 7 and Figure 8.

Primary interface estimation: The main idea in this step is that only the sufficiently close parts of each bone have cartilages attached to them. Hence, we select an initial subset of the primary bone, as the *base* of the cartilage based on its distance to the secondary bone. Our choice is based on the signed distance between the face barycenters of the primary bone and the secondary bone vertices. Provided the distance filter parameter, δ , we assign this set of faces as:

$$\mathcal{F}_C^D \equiv \{\vec{f} \in \mathcal{F}_P : \min_{\vec{v} \in \mathcal{V}_S} \|\mathbf{BC}(\vec{f}) - \vec{v}\| \leq \delta\} \quad (1)$$

where $\mathbf{BC}(\vec{f})$ is the barycenter of face \vec{f} . We select the value of δ from literature providing the expected distance in the joint cavity [57]. The accuracy of the surface estimation highly depends on this value. We denote this subset of faces as \mathcal{F}_C^D . We further trim the outer boundary and discard the faces with two boundary edges to provide additional robustness to the initial guess. The trimming helps ensure the primary interface does not cross the natural ridges on the bones.

Secondary interface definition: In the next step, we define the *top* surface of the cartilages and denote the subset as \mathcal{F}_C^E . In single-piece cartilage joints this is a subset of the secondary bone, while in the double-piece cartilages, we extrude the primary interface half-way towards the secondary bone and assign it as the top surface.

Closed surface: We interpolate between the boundary of the primary and secondary interfaces to create a single closed surface ($\mathcal{V}_C, \mathcal{F}_C$).

3.4.1. Single-piece cartilage joints

Figure 7 illustrates the cartilage generation steps for the sacroiliac joint and pubic symphysis. In the sacroiliac joint, we refer to the sacrum bone as the primary bone and the hip bone as the secondary bone. In the pubic symphysis, the left hip is considered as the primary bone and the right hip is the secondary bone.

Primary and Secondary interface estimation. The geometry of the primary and secondary bones in the sacroiliac joint and pubic symphysis have well-defined ridges close to these two joint space. Thanks to this structure, these bones are sensitive to the distance filtering parameter and allow an accurate estimation of the primary and secondary interfaces. In Figure 7 the primary and secondary interfaces for both the joints are shown with blue and green, respectively.

Closed surface. Next, we connect the primary and secondary interfaces with triangle meshes. Denoting the border of \mathcal{F}_C^D as Γ_C^D , and \mathcal{F}_C^E as Γ_C^E , we construct a mesh layer between Γ_C^D and Γ_C^E by applying a sweep-line technique [58]. Given the borders of the two interfaces, the sweep line algorithm passes an imaginary line through the border nodes and builds a discretized plane between them (\mathcal{F}_C^R). Figure 7 illustrates this connecting ring in pink. As a final step, we invert the triangles in the primary interface and merge the three disjoint subsets ($\mathcal{F}_C^D, \mathcal{F}_C^E$, and \mathcal{F}_C^R) into a single mesh. Observe the closed surfaces in Figure 9.

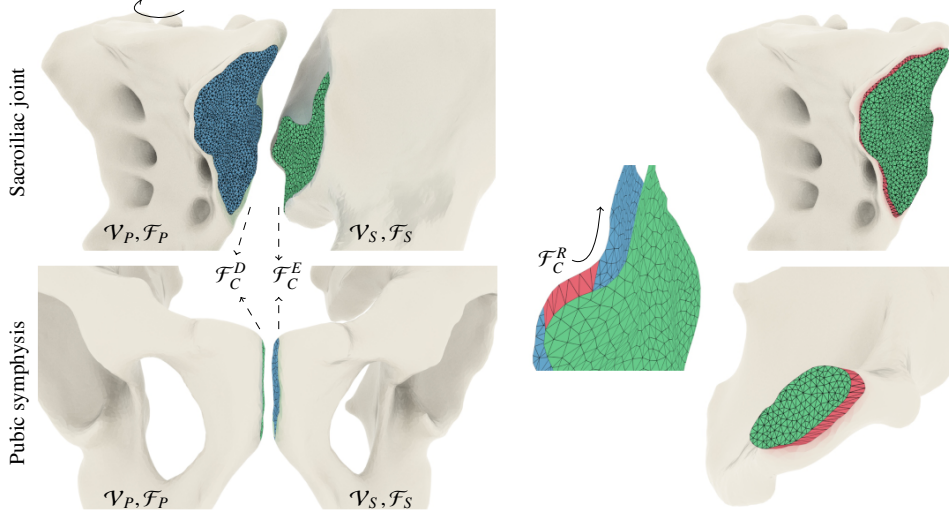


Figure 7: The cartilage generation procedure for the sacroiliac joint and the pubic symphysis; The primary and secondary bones are shown with $\mathcal{V}_P, \mathcal{F}_P$ and $\mathcal{V}_S, \mathcal{F}_S$, respectively. The cartilage base starts from the primary bone and extrudes to the secondary bone. The blue and green surfaces indicate the primary (\mathcal{F}_C^D) and secondary interface estimations (\mathcal{F}_C^E), respectively. These subsets are selected based on the distance to the opposite bone (Eq. (1)). The pink ring indicates the connecting mesh between the two interfaces (\mathcal{F}_C^R).

3.4.2. Double-piece cartilage joints

Figure 8 illustrates the cartilage generation procedure in the hip joint cavity. We generate one cartilage attached to the acetabulum bone and one attached to the femoral head bone. The acetabular cartilage is in line with the lunate surface of the acetabulum, and the femoral cartilage covers most of the femoral head, excluding the fovea pit [17]. These two cartilages follow the same curvature and thin out as they get closer to their borders. Focusing on the femoral cartilage, we describe the femur as the primary bone ($\mathcal{V}_P, \mathcal{F}_P$) and the hip as the secondary bone ($\mathcal{V}_S, \mathcal{F}_S$). On the acetabular side, the primary and secondary bones are swapped, assuming the hip as the primary and the proximal femur as the secondary bones.

Primary interface estimation. The lunate surface forms a plateau in the acetabulum bone; Thanks to this structure, the hip side is sensitive to the distance filtering parameter (δ), allowing an accurate estimation of the primary interface. The initial estimation on the femoral side does not yet comprehensively cover the femoral head. We observe the femoral cartilage border as a change in the curvature between the femoral head and the femoral neck. Thus, we further apply a curvature-based region filling approach to grow the initial guess to the correct portion on the femoral head. The details of this step can be found in [15]. Figure 8 illustrates the initial and the final primary interfaces on the femur in yellow and blue color, respectively.

Secondary interface definition. We assign a thickness profile to the primary interfaces to create the top surface of the cartilage. We make a copy of \mathcal{F}_C^D and denote it as the extruding surface (\mathcal{F}_C^E). Initially, we select a subset of \mathcal{F}_C^E and extrude it towards the secondary bone as:

$$\vec{v} \leftarrow \vec{v} + \frac{1}{2} \vec{n} \min_{\vec{v}_s \in \mathcal{V}_S} \|\vec{v} - \vec{v}_s\|_2 \quad (2)$$

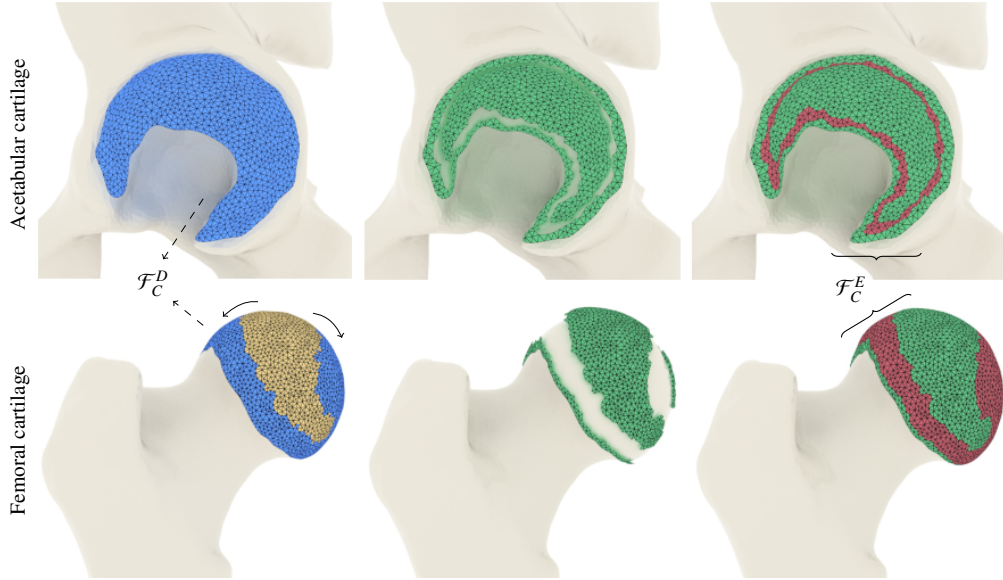


Figure 8: The acetabular and femoral cartilage generation in the hip joint; The blue surface indicates the primary interface estimation on the bones \mathcal{F}_C^D . This subset is selected based on the distance to the opposite bone. The initial primary estimation in the femur bone (yellow) does not comprehensively cover the femoral head. Thus, we apply a curvature-based region filling to grow the yellow cartilage to the correct portion on the femoral head (blue). We make a copy of the primary interface to create the top surface of the cartilage \mathcal{F}_C^E . We initially extrude a part of this surface to a maximum of half the distance to the second bone (green) and then connect the extruded subsets via a smooth blend (pink).

Where \vec{n} is the unit outward normal direction of vertex \vec{v} in \mathcal{F}_C^D . The number $1/2$ describes the extrusion height which is equal to the mid-distance between the two bone. This guarantees congruency between the cartilage-cartilage interface. To ensure an excellent blending profile in the corners, we extrude the border meshes based on a sin function. These two surfaces are shown in green in Figure 8.

We connect the two extruded subsets via a smooth blend. We apply a *biharmonic weighting* scheme to compute a blended extrusion on the remaining of \mathcal{F}_C^E which we did not initially select for extrusion. This subset is shown in pink color in Figure 8. A detailed explanation of this blending method is available at [59].

Closed surface. We invert the triangles in the primary interface and combine it with the secondary interface into a single mesh. Observe the closed surfaces in Figure 9. As explained in Section 2.3.1, we provide two versions of hip joint models for each subject: with and without a gap between the articular cartilages. This can be done by controlling the extrusion height when defining the top surface. We found that reducing the extrusion height from the midpoint 0.5 to 0.45 leaves a small gap between the two articular cartilages. In this version, the cartilages will come into contact after applying a load in the FE simulation. The joint congruency level is measured using the distance between the acetabular and femoral cartilages.

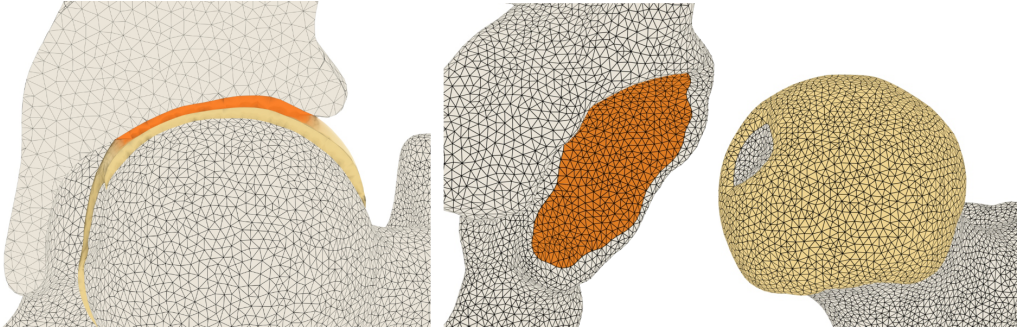


Figure 9: The reconstructed hip joint cartilages on the acetabular (orange) and femoral (yellow) sides; The acetabular cartilage is in-line with the lunate surface of the acetabulum, and the femoral cartilage covers most of the femoral head, excluding the fovea pit [17]. The cartilages have congruent interfaces and thin out as they get closer to their borders.

3.5. Volume mesh generation

We employ the same meshing tool introduced in Section 3.3.1 to generate volume meshes for three reasons: 1) We want to have control over mesh size in our models and have the option to generate coarser meshes than the input mesh size; 2) Even though all the shared interfaces in our surface mesh models are conforming by design, we still need to ensure these properties are preserved after the volume mesh generation; 3) We want high geometrical accuracy after volume mesh generation.

Using fTetWild [37], we create volume mesh for all the sub-domains simultaneously rather than building our discretized model one by one. fTetWild constructs volume meshes inside and outside the model, filling a bounding box around the model. Figure 10 shows the raw output of fTetWild. These tetrahedrons still have no inside/out classification. We apply a post-processing step to extract the interior volume of each object and filter out the elements that do not belong to any of the objects. This procedure is demonstrated in Figure 10. We calculate the signed distance of the centroid of each tetrahedron toward the surface of each object. If the signed distance is below zero, we consider that tetrahedron inside that particular object. The tetrahedrons, which have no negative signed distance towards any of the objects in our model, are filtered out before exporting the final mesh.

We deliver two mesh densities for each subject: *Fine* and *coarse* meshes. The reason is to show that our pipeline can provide different mesh resolutions depending on the users' computational resources. We calibrate the *ideal edge length* (l) parameter in fTetwild to have larger elements in the coarse version [37] and smaller elements in the fine version. We further select a small *epsilon value* (ϵ) value to preserve the anatomical details in both versions. The meshing parameters and the number of elements in each model are provided in Section 4.2.

3.5.1. Mesh quality

We ensure that the final volume mesh elements are in good quality with no flat elements. The most convenient approach involves the dihedral angles, which is the angle between adjacent facets in a tetrahedral. We expect to see no dihedral angle close to 0° or 180° [60]. We employ a method proposed by Freitag et al. to define the lower and upper bound of the dihedral angle as:

$$\min\{30^\circ, \theta_{min} + 10^\circ\} < \theta < \max\{150^\circ, \theta_{max} - 20^\circ\} \quad (3)$$

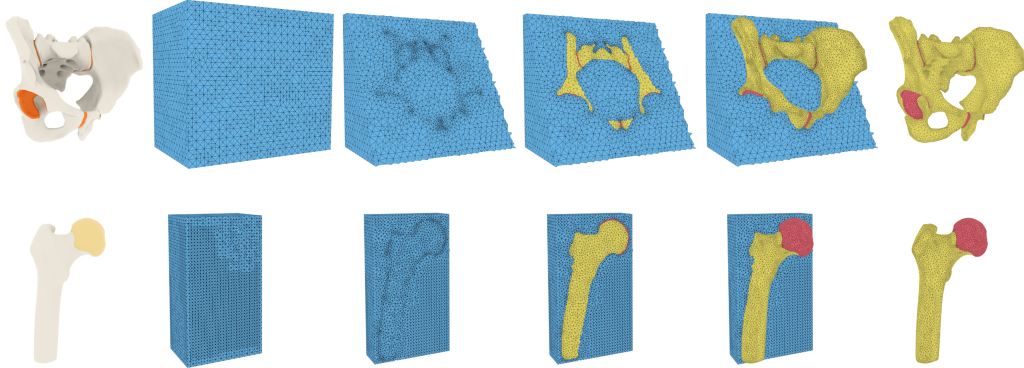


Figure 10: Overview of the fTetWild volume mesh generation; The raw output is a tetrahedral mesh of the bounding box. This volume yet has no inside/outside classification. We apply a post-processing step to filter out the exterior volume and keep the interior elements in each sub-domain. The volume mesh is extracted using the signed distance measure w.r.t the input surface. Negative and positive distances indicate interior and exterior elements, respectively.

where θ_{min} and θ_{max} denote the minimal and maximal dihedral angle in our models and θ is the dihedral angle of each element. To give quantitative information about the number of poor elements we provide the percentage of dihedral angles falling out of this range.

Further, we test the robustness of our discretization results by checking other quality metrics suggested in literature. These include the volume-edge ratio (Q_{ve}) [61], the radius ratio (Q_{rl}) [62], and the volume-area ratio (Q_{ra}) [63].

3.6. Finite element simulation

We use the two FE solvers described in Section 2.3.1. We demonstrate the usability of our models with the off-the-shelves FEBio solver, and we study the importance of bilateral modeling in the hip joint area using PolyFEM. A pseudo-stance scenario under dynamic structural mechanics analysis is setup in both the solvers and the von Mises stress is calculated as the direct simulation output. Since the deformation of the bone is negligible under a pseudo-stance position, we consider the bone to be homogeneous. The bones and cartilages are presented by the Neo-Hookean elastic material model. The material properties for both experiments are from literature [5]: The Elastic modulus (E) for the bones and cartilages is $17GPa$ and $12MPa$, respectively, and the Poisson's ratio (ν) is equal to 0.30 and 0.45, respectively.

Experiment A: Simulation performance of the FE models using FEBio

The purpose of this experiment is to test the mesh quality of all our models in FE simulation. We model a pseudo-stance scenario by fixing the pelvic girdle in the x,y, and z-direction and push the femur bones toward the pelvic girdle in the z-direction. The femur bones have restricted displacement and rotation in the x and y-direction and we apply a load equal to the bodyweight to the distal end of the femoral bones. This load starts from zero and increases linearly to $250N$ on each femur. An augmented surface contact algorithm with friction-less tangential interaction is applied between the articular interfaces allowing unhindered motion in the hip joint.

Experiment B: Effect of bilateral modeling using PolyFEM

As explained in Section 2, most of the hip joint population-based studies use the geometry of only one side of the body and apply the effect of the other side as boundary conditions [19, 29]. In this experiment, we investigate the importance of accounting for both sides of the body in a FE analysis. We set the same pseudo-stance scenario as in the first experiment and apply a prescribed displacement equal to $1mm$ to the distal end of the femoral bones towards the pelvic girdle. Then, we remove the geometry of half of the body and replace their effect by fixing the pubic symphysis and the sacroiliac attachment surfaces in the x,y, and z-direction. We assign *Tet4* elements for the bone geometries and *Tet10* elements to the cartilage tissue.

4. Results and Discussion

In this section, we present and discuss our results, starting from the accuracy of the anatomical approximations. Next, we show the mesh quality measurement results, and finally, we describe our findings from the FE simulations.

4.1. Anatomical structures

The FE models of the 11 subjects are illustrated in Figure 11. The anatomical measurements for the bones and cartilages are measured in Table 3 and Table 4, respectively. These measurements agree with the range of values reported in literature, showing proper approximations of both bony and cartilage structures.

Table 3: The Bone anatomical measurements; These measurements agree with the range of values reported in literature [53, 55, 64], showing proper approximations of the bony structures. Comparing the anatomical measurements among the 11 models indicates a considerable inter-subject variability in our study group. This differences emphasize the importance of subject-specific modeling and the role of population-based studies. The difference between the left and right side shows the bilateral variation and asymmetry in this area which has been neglected in literature (Table 1)

Model	Pelvic Girdle						Femur Bones					
	IHS	L-IH	R-IH	L-IW	R-IW	PW	L-FHSR	R-FHSR	L-FHAR	R-FHAR	L-VFL	R-VFL
m1	172.50	153.67	156.55	58.83	61.01	290.29	26.94	27.85	26.00	27.00	233.54	228.31
m2	165.14	143.00	146.14	52.07	46.15	263.16	24.99	24.87	24.00	24.00	191.11	195.21
m3	167.70	146.99	143.78	36.94	47.81	253.50	28.06	26.20	25.00	24.00	166.63	160.76
m4	171.46	143.74	140.53	49.67	37.35	258.64	25.49	26.19	25.00	25.00	167.73	184.26
m5	180.79	151.50	147.85	60.41	68.32	309.08	27.99	27.54	27.00	27.00	201.21	190.27
m6	169.86	142.01	138.38	40.84	53.77	264.45	25.31	26.49	24.00	25.00	129.86	122.29
m7	169.67	132.31	130.94	48.55	44.90	263.20	27.25	23.63	25.00	23.00	92.03	92.50
m8	192.73	161.85	155.12	54.29	58.78	305.96	26.50	27.78	25.00	27.00	153.37	157.99
m9	185.21	157.23	151.38	58.65	54.73	298.58	28.30	28.54	27.00	27.00	110.55	113.15
m10	174.39	153.46	151.75	50.77	54.87	278.11	25.82	25.62	25.00	25.00	90.75	100.11
m11	187.36	152.92	151.21	46.33	49.57	283.22	26.67	27.08	25.00	26.00	97.84	92.82
<i>Mean</i>	176.09	148.97	146.69	50.67	52.48	278.93	26.67	26.53	25.27	25.45	148.60	148.88
<i>SD(±)</i>	8.60	7.93	7.39	7.07	8.16	18.92	1.11	1.38	0.96	1.37	46.15	45.05

Comments: IHS: Inter-hip separation; L-, R-IH: height of the left and right ilium; L-, R-IW: width of the left and right ilium; PW: the width of the pelvis (PW); L-, R-FHSR: the left and right femoral head sphere radius; L-, R-FHAR: the left and right femoral head actual radius; L-, R-VFL: the left and right visible femur length

For example, our models' mean femoral and acetabular cartilage thickness is equal to $1.38mm$ and $1.64mm$, respectively. These numbers fall in the same range of $1.15-1.6mm$ for the acetabular cartilage, and $1.18-1.78mm$ for the femoral cartilage [18, 65–67]. The mean inter-hip separation, the ilium height and width is $\approx 176.09mm$, $147.83mm$, and $51.57mm$, respectively. These values are close to $202.20mm$, $152.50mm$, and $58.60mm$ from literature [53].

Comparing the overall shape and the anatomical measurements among these 11 models indicates a considerable inter-subject variability in our study group. These differences emphasize

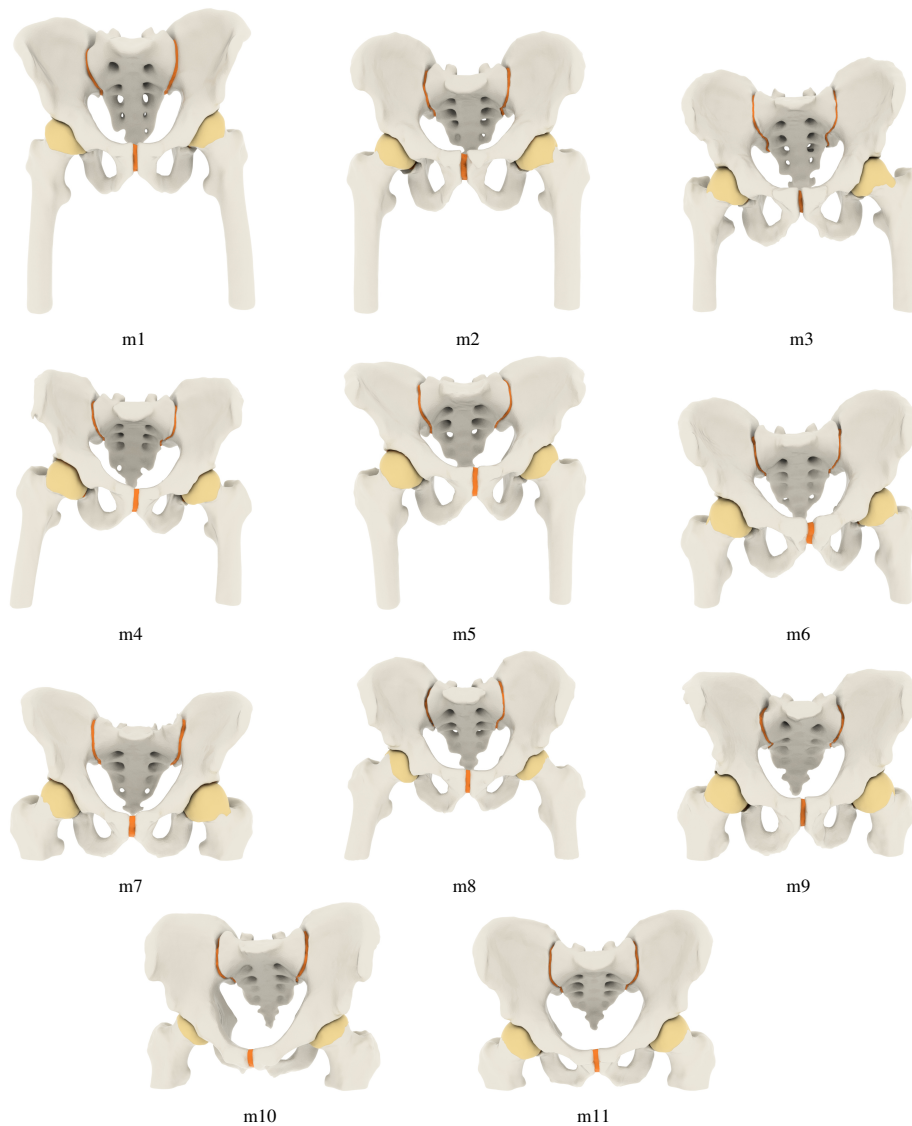


Figure 11: Subject-specific Finite element models of 11 male subjects with no diagnosed diseases related to the hip joint. Each model consists of the sacrum, the paired hip bones, the paired proximal femurs, the paired sacroiliac joints, the pubic symphysis, and the paired hip joints. The bones are directly derived from the CT scans, and the cartilages are generated subject-specifically independent of the CT scans. Comparing the overall shape and the anatomical measurements among these 11 models indicates a considerable inter-subject variability in our study group. Besides, the difference between the left and right sides of the body shows the bilateral variation and asymmetry in the hip joint area.

the importance of subject-specific modeling and geometrical variation in FE studies. Further, the difference between the models' left and right sides shows the bilateral variation and asymmetry in this area which has been neglected in some studies [3]. In Figure 12, we compare a spherical head shape with a subject-specific femoral head. The difference between the radius of these two

Table 4: The joint anatomical measurements; These measurements agree with the range of values reported in literature [18, 65–68], showing proper approximations of the cartilage structures. Comparing the anatomical measurements among the 11 models indicates a considerable inter-subject variability in our study group. These differences emphasize the importance of subject-specific modeling and the role of population-based studies. The difference between the left and right sides shows the bilateral variation and asymmetry in this area, often neglected in FE simulations.

Model	HJ-Acetabulum		HJ-Femur		Sacroiliac Joint			Pubic symphysis		
	Avg.T (w/wo gap)	BCA	Avg.T (w/wo gap)	BCA	Avg.T	PB-CA	SB-CA	Avg.T	PB-CA	SB-CA
m1	1.11 / 1.23	2914.16	1.33 / 1.61	5753.90	5.13	2401.30	2381.49	2.05	475.53	492.63
m2	1.33 / 1.48	2515.68	1.58 / 1.83	4808.44	5.06	1930.80	2028.47	2.89	338.92	301.79
m3	0.95 / 1.06	2236.36	1.05 / 1.17	4849.46	3.58	1696.37	1808.11	1.46	268.58	268.96
m4	1.26 / 1.40	2758.58	1.43 / 1.61	5465.50	4.16	1864.25	1982.89	3.86	411.19	416.17
m5	1.23 / 1.37	2998.12	1.44 / 1.64	5866.13	4.60	2701.15	2831.03	2.23	517.00	538.50
m6	1.29 / 1.45	2208.21	1.36 / 1.54	4831.51	4.21	1310.26	1419.71	2.30	337.80	309.89
m7	1.40 / 1.56	2198.43	1.56 / 1.86	4608.98	5.88	2048.43	2136.46	3.04	352.19	369.18
m8	1.47 / 1.63	2941.67	1.54 / 1.75	5325.95	5.38	2484.03	2552.02	2.45	351.36	353.73
m9	1.59 / 1.77	2819.23	1.62 / 2.01	6111.12	4.71	2332.81	2447.49	1.77	461.99	494.80
m10	1.64 / 1.82	2266.76	1.41 / 1.56	4950.50	6.30	2451.53	2550.57	2.48	559.05	555.34
m11	1.17 / 1.30	2240.89	1.28 / 1.43	5051.55	4.96	2245.62	2396.42	2.21	365.42	340.60
<i>Mean</i>	1.31 / 1.46	2554.37	1.42 / 1.64	5238.46	4.91	2133.32	2230.42	2.43	403.55	403.78
<i>SD(±)</i>	0.20 / 0.22	318.85	0.16 / 0.22	476.38	0.75	388.46	382.65	0.62	84.87	96.55

Comments: Avg.T: average thickness; w/wo: with and without gap between the articular cartilages in the hip joint; BCA: bone coverage area; PB-CA: the primary bone coverage area; SB-CA: the secondary bone coverage area;

demonstrates how the geometry of the femoral head deviates from a sphere, and the amount of subject-specific data one loses when simplifying the femoral bone.

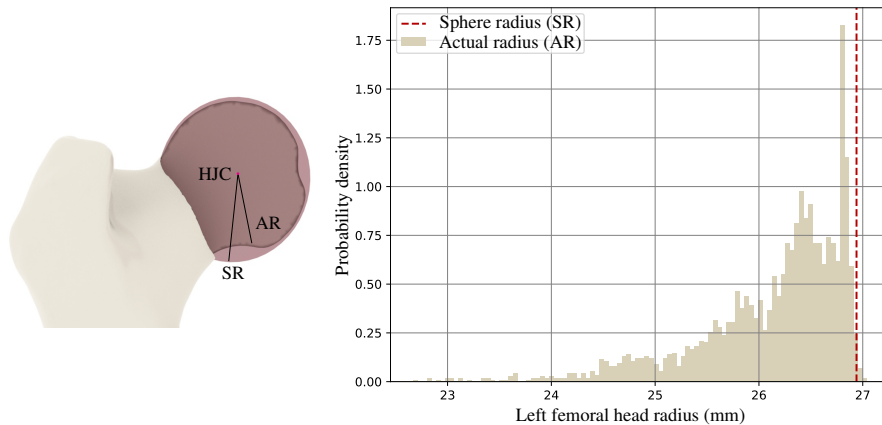


Figure 12: The comparison between the spherical and detailed design of the femoral head; We fit a sphere to the femoral head, and the sphere’s diameter is defined as the simplified femoral head radius (SR). We define the distance between the sphere’s center (HJC) and the femoral head boundary as the actual femoral head radius (AR). The variation of AR in subject *m1* is shown as a probability density, and SR is shown with a red line. The red line and the beige distribution indicate the amount of subject-specific data lost when simplifying the femoral head with a sphere.

Our modeling workflow is implemented in Python, mainly using the Libigl library [69]. To quantify the speed of the cartilage generation for each subject, we time all the steps described in Section 3.4 to generate the two hip joints, the two sacroiliac joints, and the pubic symphysis. The geometry processing is done using a MacBook Pro 2018 with a 2.7 GHz quad-core Intel i7. We observe that, on average, the cartilage reconstruction takes 4 minutes for each subject. While this time is significantly short, generating *good* cartilages can take longer as we need to calibrate the free parameters in the cartilage generation pipeline [15]. These parameters did not deviate

significantly among our subjects, so minimal time was needed for parameter tuning.

It should be noted that our cartilage generation algorithm is sensitive to the geometry of the input bone mesh. Any bone abnormalities or segmentation errors affect the cartilages' final shape. For example, even though there was no reported information regarding diseased hip joints, we found that some subjects, such as *m4* have a *hip cam impingement* which is a bump close to the femoral head. As we generate the femoral cartilage based on the femur bone curvatures, this bone abnormality affects the shape of the cartilage boundary.

4.2. Mesh quality

Table 5 summarizes the volume mesh properties of each subject in both the fine and coarse versions. In the fine and coarse models, the Hausdorff distance between the surface boundary before and after volume mesh generation is, on average, 0.16 and 0.17(*mm*), respectively. To better understand the Hausdorff distance size, we additionally present it in percentage terms. We divide this distance by the diagonal of the bounding box in the initial surface and denote it by $\% \Delta$. The average percentage of 0.04 indicates highly-accurate geometries.

The mean *dihedral angle* of 70.28° and 70.32° in Table 5 indicates high-quality elements. On average, the percentage of the low-quality elements in fine and coarse models are 0.00% and 0.04%, respectively. This number is less than 1%, which is negligible compared to the total number of meshes in the model. The normalized quality histogram of the other metrics is presented in Figure 13. The histograms are tilted towards one, with an insignificant number of elements close to zero. The number of elements starts growing around 0.4, indicating high-quality elements based on these measures.

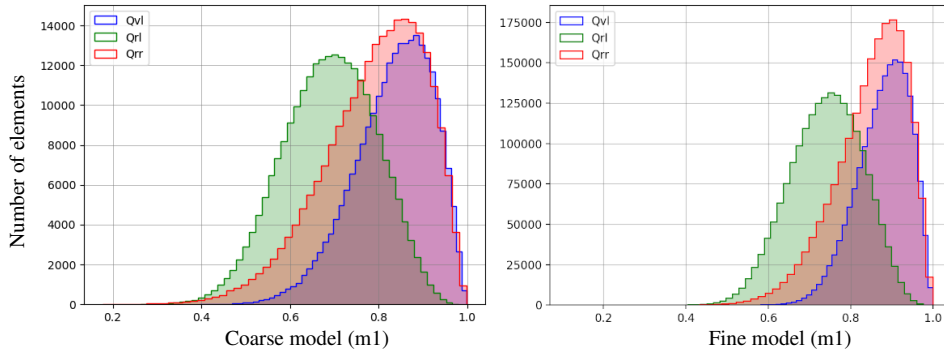


Figure 13: Normalized mesh quality histogram for model *m1*, in coarse and fine version. The quality metrics include the volume-edge ratio (Q_{vl}) in blue [61], the radius ratio (Q_{rl}) in green [62], and the volume-area ratio (Q_{rr}) in red [63]. The closer the distribution to one, the higher the mesh quality we have.

4.3. FE simulation results

The von Mises stress results in *Experiment A* is illustrated in Figure 14 for all the 11 hip joints. We use a MacBook Pro 2018 with a 2.7 GHz quad-core Intel i7 to run the simulations. Each simulation takes around 5 minutes in FEBio to converge. We experienced no convergence issues related to the discretized geometries. Even though all the subjects have the same FE simulation setup, we observe that the differences in the bone and cartilage geometries affect the stress

Table 5: The volume mesh properties of our models, in fine (F) and coarse (C) resolution; The fTetWild parameters allow preserving the anatomical details and controlling the element size. We calibrate l to have larger and smaller elements in the coarse and fine versions, respectively. We use the dihedral angle θ to quantify the quality of the elements. To better understand the amount of low-quality elements in each model, we provide the percentage of dihedral angles falling out of the accepted range. The Hausdorff distance (HD) shows how the geometry is changed after the volume mesh generation. We also present it in percentage terms to better understand the Hausdorff distance size; We divide this distance by the diagonal of the bounding box in the initial surface and denote it by $\% \Delta$. The average of the results is shown in **Bold**, indicating high-quality discretization with accurate geometries.

Models	fTetWild parameters		# of elements	Mesh quality- Q_θ				Geometrical accuracy	
	ϵ	l		Mean θ	SD	$\% \theta <$	$\% \theta >$	HD (mm)	($\% \Delta$)
m1 , F	5e-4	0.007 / 0.006	2.0M	70.26	17.45	0.03	0.00	0.14	0.03
m1 , C	5e-4	0.024 / 0.020	192K	70.36	21.41	0.84	0.08	0.14	0.03
m2 , F	5e-4	0.007 / 0.006	2.2M	70.28	17.09	0.03	0.00	0.30	0.07
m2 , C	5e-4	0.024 / 0.020	264K	70.35	19.61	0.44	0.00	0.17	0.04
m3 , F	5e-4	0.007 / 0.006	2.6M	70.20	17.18	0.04	0.00	0.13	0.03
m3 , C	5e-4	0.024 / 0.018	260K	70.34	21.08	0.40	0.17	0.26	0.06
m4 , F	5e-4	0.007 / 0.006	2.6M	70.27	17.21	0.01	0.00	0.13	0.03
m4 , C	5e-4	0.024 / 0.020	223K	70.36	20.97	0.44	0.10	0.14	0.03
m5 , F	6e-4	0.007 / 0.006	2.5M	70.29	17.59	0.02	0.00	0.19	0.04
m5 , C	6e-4	0.024 / 0.018	204K	70.32	20.55	0.62	0.11	0.28	0.06
m6 , F	5e-4	0.007 / 0.006	3.6M	70.28	17.61	0.01	0.00	0.15	0.04
m6 , C	5e-4	0.024 / 0.018	274K	70.30	20.16	0.46	0.08	0.14	0.03
m7 , F	5e-4	0.007 / 0.006	5.2M	70.29	17.23	0.01	0.00	0.14	0.04
m7 , C	5e-4	0.024 / 0.018	341K	70.26	19.14	0.44	0.05	0.14	0.04
m8 , F	5e-4	0.007 / 0.006	3.2M	70.27	17.40	0.01	0.00	0.18	0.04
m8 , C	5e-4	0.024 / 0.020	251K	70.35	20.71	0.47	0.12	0.16	0.03
m9 , F	5e-4	0.007 / 0.006	4.6M	70.28	17.54	0.02	0.00	0.15	0.03
m9 , C	5e-4	0.022 / 0.018	326K	70.28	19.58	0.63	0.09	0.17	0.04
m10 , F	5e-4	0.007 / 0.006	5.3M	70.32	17.50	0.01	0.00	0.15	0.03
m10 , C	5e-4	0.024 / 0.020	326K	70.32	19.88	0.36	0.06	0.15	0.03
m11 , F	5e-4	0.007 / 0.006	4.8M	70.30	17.26	0.01	0.00	0.14	0.03
m11 , C	5e-4	0.024 / 0.020	299K	70.29	19.95	0.63	0.08	0.16	0.04
<i>Avg.F</i>	5e-4	0.007 / 0.006	3.5M	70.28	17.37	0.02	0.00	0.16	0.04
<i>Avg.C</i>	5e-4	0.024 / 0.019	269K	70.32	20.28	0.52	0.04	0.17	0.04

ϵ : Envelop of size epsilon; l : Ideal edge length; Mean: Mean dihedral angle; SD: Standard deviation; Q_θ : The dihedral angle mesh quality metric; $\% \theta <$ and $\% \theta >$: Percentage of elements which their dihedral angle falls below or above the range of good quality tetrahedrals, respectively; HD: The Hausdorff Distance; $\% \Delta$: The percentage of the HD w.r.t. the bounding box.

distribution pattern and values across the subjects. The stress distribution pattern in these joints shows no spurious stress peaks and gradual changes in the joint cartilages. The stress ranges between 0 – 0.62 (MPa) in the hip joint cartilages, which is lower than the reported values in the literature [5]. The reason is that these models are in the supine position. To get similar results, we need to first re-locate the femur and hip bones to the *neutral* position. However, the purpose of our simulations is only to verify the simulation properties of our FE models.

The difference between the one-sided models and the bilateral models in *Experiment B*. is presented in Figure 15. We use a workstation with an AMD Ryzen Threadripper PRO 3995WX CPU. We use a max of 16 threads, which leads to a runtime of around 130 minutes for each simulation. The significant difference in the von Mises stress values and pattern justifies that it is an invasive approach to only include half of the body when studying the hip joint behavior. These results suggest that such simplified studies as in [19, 29] may lead to under/overestimations regarding the stress values.

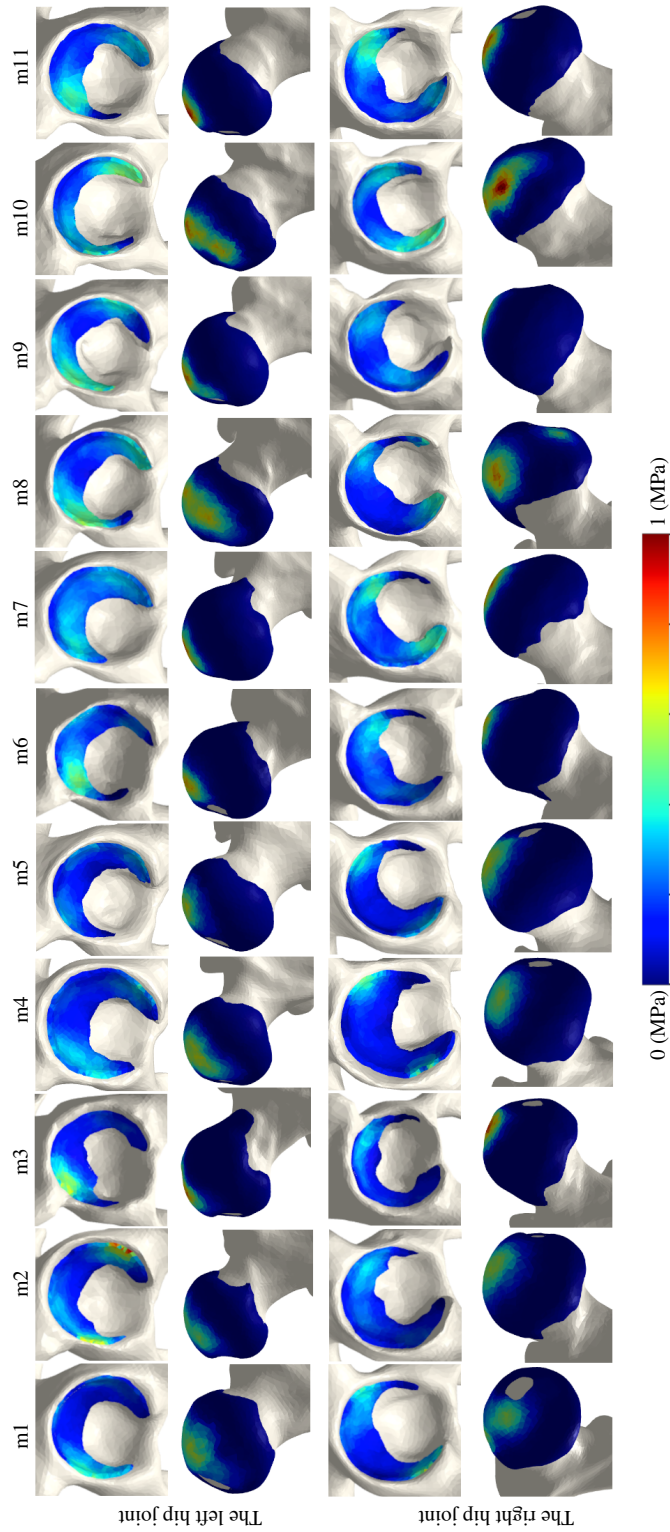


Figure 14: The FE analysis results in the hip joint; The color bar shows the normalized von Mises stress in the hip joint cartilages. Even though all the subjects have the same FE simulation setup, we observe that the differences in the bone and cartilage geometries affect the stress distribution pattern and values across the subjects. The stress distribution pattern in these joints shows no spurious stress peaks and gradual changes in the joint cartilages. The overall stress values range from $0 - 0.62(\text{MPa})$.

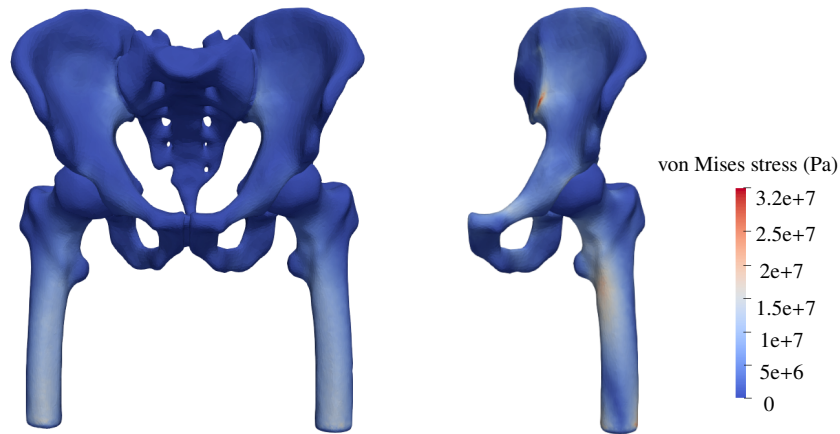


Figure 15: The comparison between simulation results of bilateral modeling and one-side hip joint models; The model in the left image covers both sides of the body, while in the right image, we only have the geometry of the left side, and the effect of the rest of the body is applied as boundary conditions on the hip bone. The significant difference in the von Mises stress value and pattern justifies that it is an invasive approach to only include half of the body when studying the hip joint behavior, which may lead to unrealistic estimations. Note that the stress values are to compare the output differences and may not be realistic as the simulation setup is still a pseudo-stance.

5. Conclusion and Future work

Our work aimed to provide multiple subject-specific finite element models of the hip joint for simulation purposes. We provide verified bilateral models covering the bones and cartilages in the hip joint area. Our models allow scientists to account for the inter-subject and bilateral variability when studying the hip joint behavior. The FE analysis experiments in this work qualify the usability of our models in FE simulations. We have made different versions of each subject to ensure the models are compatible with different FE method solvers and scenarios. We suggest that it is not suitable to only use a single subject in the FE analyses, and it is an invasive assumption to replace geometries by their effects as boundary conditions.

Our modeling pipeline and geometry processing codes are available on GitHub [14]. The codes cover the input bone re-meshing process, the cartilage generation process, the multi-body volume generation process, the mesh quality assessment codes, and a sample FEBio model file generator. Even though the FE models are the main output in our work, one can use each section's initial input and output separately for other purposes. For example, the CT scan segmentation label maps can be used as training data to develop automated bone segmentation models.

Additionally, the pipeline is compatible with adding more data or replacing each section. For example, additional bone segmentation can be added to the pipeline's input to develop more FE models. One can also directly segment the cartilages from image modalities, replace them with the generated cartilages in our method, and still generate high-quality FE models. The concept behind our pipeline is not limited to the hip joint only, and similar concepts can be applied to the jaw dataset or dental applications [70].

The proposed cartilage generation method in our modeling workflow is fast and generates proper cartilages. However, we must note that our cartilage generation method is sensitive to the input bone geometries, and any abnormalities or segmentation errors may lead to less accurate

results. The surface and volume discretizations have been proved to have high-quality elements using several mesh quality metrics. An outstanding feature of these models is that we have conforming interfaces in our multi-body models. Thus, one does not need to manually define *fixed contact definitions* in the bone-cartilage interfaces when running simulations. Further, the high congruency level between the articular cartilages in the hip joint allows a smooth transition of force in the hip joint, leaving no stress peaks due to improper cartilage geometries.

The von Mises stress results reported in our work only serve as a quality test of simulation properties. We need a more advanced simulation setting to model a real stance position, such as proper material properties. This explains the difference in the stress values compared to the literature. Moreover, all the subjects in our work are in the supine position during the image acquisition. They are lying down on the scanning tray, and the relative location of the femur and hip bones are affected by this position. One solution is to relocate the bone geometries to a *neutral* position before setting up any custom simulations setup. We leave this for future work. Future work could extend to using these FE models to estimate the stress distribution in a complete gait cycle. Our models currently lack other soft tissues. Future work can add more structures in the hip joint area, such as the hip joint labrum, capsule, and ligaments.

Declaration of Competing Interest

The authors declare that they have no known competing financial interests or personal relationships that could have appeared to influence the work reported in this paper.

Funding

This project has received funding from the European Union’s Horizon 2020 research and innovation programme under the Marie Skłodowska-Curie grant agreement No. 764644. This paper only contains the author’s views, and the Research Executive Agency and the Commission are not responsible for any use that may be made of the information it contains.

This work was partially supported by the NSF CAREER award under Grant No. 1652515, the NSF grants OAC-1835712, OIA-1937043, CHS-1908767, CHS-1901091, NSERC DGEGR-2021-00461 and RGPIN-2021-03707, a Sloan Fellowship, a gift from Adobe Research and a gift from Advanced Micro Devices, Inc.

Acknowledgements

We thank the NYU IT High Performance Computing for resources, services, and staff expertise. We would also like to thank Christos Koutras, Niels-Christian Borbjerg, and Rasmus Netterstrøm for their valuable feedback and contribution to our work.

References

- [1] M. Baccouch, A brief summary of the finite element method for differential equations, in: *Finite Element Methods and Their Applications*, IntechOpen, 2021.
- [2] C. F. SCIFERT, T. D. BROWN, D. R. PEDERSEN, A. D. HEINER, J. J. CALLAGHAN, Development and physical validation of a finite element model of total hip dislocation, *Computer methods in biomechanics and biomedical engineering* 2 (2) (1999) 139–147.

- [3] X. Zhao, E. Chosa, K. Totoribe, G. Deng, Effect of periacetabular osteotomy for acetabular dysplasia clarified by three-dimensional finite element analysis, *Journal of orthopaedic science* 15 (5) (2010) 632–640.
- [4] R. A. Salmingo, T. L. Skytte, M. S. Traberg, L. P. Mikkelsen, K.-Å. Henneberg, C. Wong, A method to investigate the biomechanical alterations in perthes' disease by hip joint contact modeling, *Bio-medical materials and engineering* 28 (4) (2017) 443–456.
- [5] B. Vafaeian, D. Zonoobi, M. Mabee, A. Hareendranathan, M. El-Rich, S. Adeeb, J. Jaremko, Finite element analysis of mechanical behavior of human dysplastic hip joints: a systematic review, *Osteoarthritis and cartilage* 25 (4) (2017) 438–447.
- [6] Z. Zou, A. Chávez-Arreola, P. Mandal, T. N. Board, T. Alonso-Rasgado, Optimization of the position of the acetabulum in a ganz periacetabular osteotomy by finite element analysis, *Journal of Orthopaedic Research* 31 (3) (2013) 472–479.
- [7] N. Vaughan, V. N. Dubey, T. W. Wainwright, R. G. Middleton, A review of virtual reality based training simulators for orthopaedic surgery, *Medical engineering & physics* 38 (2) (2016) 59–71.
- [8] B. Helgason, H. Pálsson, T. P. Rúnarsson, L. Frossard, M. Viceconti, Risk of failure during gait for direct skeletal attachment of a femoral prosthesis: a finite element study, *Medical engineering & physics* 31 (5) (2009) 595–600.
- [9] D. Kluess, R. Souffrant, W. Mittelmeier, A. Wree, K.-P. Schmitz, R. Bader, A convenient approach for finite-element-analyses of orthopaedic implants in bone contact: modeling and experimental validation, *Computer methods and programs in biomedicine* 95 (1) (2009) 23–30.
- [10] K. Chethan, N. S. Bhat, M. Zuber, B. S. Shenoy, Finite element analysis of hip implant with varying in taper neck lengths under static loading conditions, *Computer Methods and Programs in Biomedicine* 208 (2021) 106273.
- [11] W. Zeng, Y. Liu, X. Hou, Biomechanical evaluation of internal fixation implants for femoral neck fractures: A comparative finite element analysis, *Computer Methods and Programs in Biomedicine* 196 (2020) 105714.
- [12] M. Taylor, R. Bryan, F. Galloway, Accounting for patient variability in finite element analysis of the intact and implanted hip and knee: a review, *International journal for numerical methods in biomedical engineering* 29 (2) (2013) 273–292.
- [13] M. D. Wilkinson, M. Dumontier, I. J. Aalbersberg, G. Appleton, M. Axton, A. Baak, N. Blomberg, J.-W. Boiten, L. B. da Silva Santos, P. E. Bourne, et al., The fair guiding principles for scientific data management and stewardship, *Scientific data* 3 (1) (2016) 1–9.
- [14] F. Moshfeghifar, T. Gholamalizadeh, Z. Ferguson, T. Schneider, M. B. Nielsen, D. Panozzo, S. Darkner, K. Erleben, Libhip: An open-access hip joint model repository suitable for finite element method simulation, *Online' repository*, <https://diku-dk.github.io/libhip/> (March 2022).
- [15] F. Moshfeghifar, M. K. Nielsen, J. D. Tascón-Vidarte, S. Darkner, K. Erleben, A direct geometry processing cartilage generation method using segmented bone models from datasets with poor cartilage visibility (2022). [arXiv:2203.10667](https://arxiv.org/abs/2203.10667).
- [16] M. Duprez, S. P. A. Bordas, M. Bucki, H. P. Bui, F. Chouly, V. Lleras, C. Lobos, A. Lozinski, P.-Y. Rohan, S. Tomar, Quantifying discretization errors for soft tissue simulation in computer assisted surgery: A preliminary study, *Applied Mathematical Modelling* 77 (2020) 709–723.
- [17] S. Standring, *Gray's anatomy e-book: the anatomical basis of clinical practice*, Elsevier, 2020.
- [18] A. E. Anderson, B. J. Ellis, S. A. Maas, J. A. Weiss, Effects of idealized joint geometry on finite element predictions of cartilage contact stresses in the hip, *Journal of biomechanics* 43 (7) (2010) 1351–1357.
- [19] C. R. Henak, C. L. Abraham, A. E. Anderson, S. A. Maas, B. J. Ellis, C. L. Peters, J. A. Weiss, Patient-specific analysis of cartilage and labrum mechanics in human hips with acetabular dysplasia, *Osteoarthritis and cartilage* 22 (2) (2014) 210–217.
- [20] F. Sichtung, J. Rossol, O. Soisson, S. Klima, T. Milani, N. Hammer, Pelvic belt effects on sacroiliac joint ligaments: a computational approach to understand therapeutic effects of pelvic belts., *Pain Physician* 17 (1) (2014) 43–51.
- [21] K. J. Stewart, D. R. Pedersen, J. J. Callaghan, T. D. Brown, Implementing capsule representation in a total hip dislocation finite element model, *The Iowa orthopaedic journal* 24 (2004) 1.
- [22] M. Ramezani, S. Klima, P. L. C. de la Herverie, J. Campo, L. Joncour, C. Rouquette, M. Scholze, N. Hammer, et al., In silico pelvis and sacroiliac joint motion: Refining a model of the human osteoligamentous pelvis for assessing physiological load deformation using an inverted validation approach, *BioMed research international* 2019.
- [23] M. E. Russell, K. H. Shivanna, N. M. Grosland, D. R. Pedersen, Cartilage contact pressure elevations in dysplastic hips: a chronic overload model, *Journal of orthopaedic surgery and research* 1 (1) (2006) 6.
- [24] C. R. Henak, E. D. Carruth, A. E. Anderson, M. D. Harris, B. J. Ellis, C. L. Peters, J. A. Weiss, Finite element predictions of cartilage contact mechanics in hips with retroverted acetabula, *Osteoarthritis and cartilage* 21 (10) (2013) 1522–1529.
- [25] H. Tsumura, N. Kaku, S. Ikeda, T. Torisu, A computer simulation of rotational acetabular osteotomy for dysplastic hip joint: does the optimal transposition of the acetabular fragment exist?, *Journal of Orthopaedic Science* 10 (2) (2005) 145–151.
- [26] B. Gilles, N. Magnenat-Thalmann, Musculoskeletal mri segmentation using multi-resolution simplex meshes with

- medial representations, *Medical image analysis* 14 (3) (2010) 291–302.
- [27] C. R. Henak, A. E. Anderson, J. A. Weiss, Subject-specific analysis of joint contact mechanics: application to the study of osteoarthritis and surgical planning, *Journal of biomechanical engineering* 135 (2).
- [28] P. Hu, T. Wu, H.-z. Wang, X.-z. Qi, J. Yao, X.-d. Cheng, W. Chen, Y.-z. Zhang, Influence of different boundary conditions in finite element analysis on pelvic biomechanical load transmission, *Orthopaedic surgery* 9 (1) (2017) 115–122.
- [29] M. D. Harris, A. E. Anderson, C. R. Henak, B. J. Ellis, C. L. Peters, J. A. Weiss, Finite element prediction of cartilage contact stresses in normal human hips, *Journal of Orthopaedic Research* 30 (7) (2012) 1133–1139.
- [30] S. Chegini, M. Beck, S. J. Ferguson, The effects of impingement and dysplasia on stress distributions in the hip joint during sitting and walking: a finite element analysis, *Journal of Orthopaedic Research* 27 (2) (2009) 195–201.
- [31] M. E. Russell, K. H. Shivanna, N. M. Grosland, D. R. Pedersen, Cartilage contact pressure elevations in dysplastic hips: a chronic overload model, *Journal of orthopaedic surgery and research* 1 (1) (2006) 1–11.
- [32] E. F. Liechti, S. J. Ferguson, M. Tannast, Protrusio acetabuli: joint loading with severe pincer impingement and its theoretical implications for surgical therapy, *Journal of orthopaedic research* 33 (1) (2015) 106–113.
- [33] V. Spitzer, M. J. Ackerman, A. L. Scherzinger, D. Whitlock, The visible human male: a technical report, *Journal of the American Medical Informatics Association* 3 (2) (1996) 118–130.
- [34] K. Clark, B. Vendt, K. Smith, J. Freymann, J. Kirby, P. Koppel, S. Moore, S. Phillips, D. Maffitt, M. Pringle, et al., The cancer imaging archive (tcia): maintaining and operating a public information repository, *Journal of digital imaging* 26 (6) (2013) 1045–1057.
- [35] Autodesk, Meshmixer, <http://www.meshmixer.com>, accessed: 2022-02-21.
- [36] T. Schneider, Y. Hu, X. Gao, J. Dumas, D. Zorin, D. Panozzo, A large-scale comparison of tetrahedral and hexahedral elements for solving elliptic pdes with the finite element method, *ACM Transactions on Graphics (TOG)* 41 (3) (2022) 1–14.
- [37] Y. Hu, Q. Zhou, X. Gao, A. Jacobson, D. Zorin, D. Panozzo, Tetrahedral meshing in the wild., *ACM Trans. Graph.* 37 (4) (2018) 60–1.
- [38] Y. Hu, T. Schneider, B. Wang, D. Zorin, D. Panozzo, Fast tetrahedral meshing in the wild, *ACM Transactions on Graphics (TOG)* 39 (4) (2020) 117–1.
- [39] S. Hang, Tetgen, a delaunay-based quality tetrahedral mesh generator, *ACM Trans. Math. Softw* 41 (2) (2015) 11.
- [40] M. Smith, ABAQUS/Standard User’s Manual, Version 6.9, Dassault Systèmes Simulia Corp, United States, 2009.
- [41] S. A. Maas, B. J. Ellis, G. A. Ateshian, J. A. Weiss, Febio: finite elements for biomechanics, *Journal of biomechanical engineering* 134 (1) (2012) 011005.
- [42] M. Li, Z. Ferguson, T. Schneider, T. Langlois, D. Zorin, D. Panozzo, C. Jiang, D. M. Kaufman, Incremental potential contact: Intersection- and inversion-free large deformation dynamics, *ACM Transactions on Graphics* 39 (4).
- [43] Z. Ferguson, M. Li, T. Schneider, F. Gil-Ureta, T. Langlois, C. Jiang, D. Zorin, D. M. Kaufman, D. Panozzo, Intersection-free rigid body dynamics, *ACM Transactions on Graphics (SIGGRAPH)* 40 (4).
- [44] T. Schneider, J. Dumas, X. Gao, D. Zorin, D. Panozzo, Polyfem, <https://polyfem.github.io/> (2019).
- [45] T. Schneider, Y. Hu, J. Dumas, X. Gao, D. Panozzo, D. Zorin, Decoupling simulation accuracy from mesh quality, *ACM transactions on graphics*.
- [46] A. E. Weber, J. A. Jacobson, A. Bedi, A review of imaging modalities for the hip, *Current reviews in musculoskeletal medicine* 6 (3) (2013) 226–234.
- [47] H. Roth, L. Lu, A. Seff, K. Cherry, J. Hoffman, S. Wang, J. Liu, E. Turkbey, R. Summers, A new 2.5 d representation for lymph node detection in ct [dataset], The Cancer Imaging Archive. Available online: <https://wiki.cancerimagingarchive.net/display/Public/CT+Lymph+Nodes> (accessed on 8 April 2021).
- [48] K. Smith, K. Clark, W. Bennett, T. Nolan, J. Kirby, M. Wolfsberger, J. Moulton, B. Vendt, J. Freymann, Data from ct colonography. the cancer imaging archive (2015).
- [49] S. Kirk, Y. Lee, F. Lucchesi, et al., Radiology data from the cancer genome atlas urothelial bladder carcinoma [tcga-blca] collection, *Cancer Imaging Arch.*
- [50] R. Kikinis, S. D. Pieper, K. G. Vosburgh, 3d slicer: a platform for subject-specific image analysis, visualization, and clinical support, in: *Intraoperative imaging and image-guided therapy*, Springer, 2014, pp. 277–289.
- [51] B. Connolly, C. Wang, Segmented CT pelvis scans with annotated anatomical landmarks (2019). URL doi:10.23698/aida/ctpel
- [52] L. Zhu, I. Kolesov, Y. Gao, R. Kikinis, A. Tannenbaum, An effective interactive medical image segmentation method using fast growcut, in: *MICCAI workshop on interactive medical image computing*, 2014.
- [53] J. Hornova, V. Kralj-Iglič, D. Pedersen, M. Daniel, Effect of patient-specific model scaling on hip joint reaction force in one-legged stance—study of 356 hips, *Acta of bioengineering and biomechanics* 19 (4).
- [54] A. M. Christensen, N. V. Passalacqua, E. J. Bartelink, *Forensic anthropology: current methods and practice*, Academic Press, 2019.
- [55] B. Mahaisavariya, K. Sithiseripratip, T. Tongdee, E. L. Bohez, J. Vander Sloten, P. Oris, Morphological study of

- the proximal femur: a new method of geometrical assessment using 3-dimensional reverse engineering, *Medical engineering & physics* 24 (9) (2002) 617–622.
- [56] V. Pratt, Direct least-squares fitting of algebraic surfaces, *ACM SIGGRAPH computer graphics* 21 (4) (1987) 145–152.
- [57] Ö. Kalenderer, A. Turgut, T. Bacaksız, E. Bilgin, M. Kumbaracı, H. A. Akkan, Evaluation of symphysis pubis and sacroiliac joint distances in skeletally immature patients: A computerized tomography study of 1020 individuals, *Acta Orthopaedica et Traumatologica Turcica* 51 (2) (2017) 150–154.
- [58] d. B. Mark, C. Otfried, v. K. Marc, O. Mark, *Computational geometry algorithms and applications*, Springer, 2008.
- [59] A. Jacobson, I. Baran, J. Popovic, O. Sorkine, Bounded biharmonic weights for real-time deformation, *ACM Trans. Graph.* 30 (4) (2011) 78.
- [60] L. A. Freitag, C. Ollivier-Gooch, Tetrahedral mesh improvement using swapping and smoothing, *International Journal for Numerical Methods in Engineering* 40 (21) (1997) 3979–4002.
- [61] M. K. Misztal, K. Erleben, A. Bargeil, J. Fursund, B. B. Christensen, J. A. Bærentzen, R. Bridson, Multiphase flow of immiscible fluids on unstructured moving meshes, *IEEE transactions on visualization and computer graphics* 20 (1) (2013) 4–16.
- [62] T. Baker, Element quality in tetrahedral meshes. 7th int, in: *Conf. on Finite Element Models in Flow Problems*, Huntsville, Alabama, 1989.
- [63] J. Shewchuk, What is a good linear finite element? interpolation, conditioning, anisotropy, and quality measures (preprint), University of California at Berkeley 2002.
- [64] P. C. Noble, J. W. Alexander, L. J. Lindahl, D. T. Yew, W. M. Granberry, H. S. Tullos, The anatomic basis of femoral component design., *Clinical orthopaedics and related research* (235) (1988) 148–165.
- [65] A. E. Anderson, B. J. Ellis, S. A. Maas, C. L. Peters, J. A. Weiss, Validation of finite element predictions of cartilage contact pressure in the human hip joint, *Journal of biomechanical engineering* 130 (5).
- [66] I. Mechlenburg, J. R. Nyengaard, J. Gelineck, K. Soballe, Cartilage thickness in the hip joint measured by mri and stereology—a methodological study, *Osteoarthritis and cartilage* 15 (4) (2007) 366–371.
- [67] A. Lazik, J. M. Theysohn, C. Geis, S. Johst, M. E. Ladd, H. H. Quick, O. Kraff, 7 tesla quantitative hip mri: T1, t2 and t2* mapping of hip cartilage in healthy volunteers, *European radiology* 26 (5) (2016) 1245–1253.
- [68] F. Schmaranzer, R. Helfenstein, G. Zeng, T. D. Lerch, E. N. Novais, J. D. Wylie, Y.-J. Kim, K. A. Siebenrock, M. Tannast, G. Zheng, Automatic mri-based three-dimensional models of hip cartilage provide improved morphologic and biochemical analysis, *Clinical orthopaedics and related research* 477 (5) (2019) 1036.
- [69] A. Jacobson, D. Panozzo, et al., libigl: A simple C++ geometry processing library, <https://libigl.github.io/> (2018).
- [70] T. Gholamalizadeh, F. Moshfeghifar, Z. Ferguson, T. Schneider, D. Panozzo, S. Darkner, M. Makaremi, F. Chan, P. L. Søndergaard, K. Erleben, Open-Full-Jaw: An open-access dataset and pipeline for finite element models of human jaw, submitted to *Computer Methods and Programs in Biomedicine*.

Appendix D

Contact modeling from images using cut finite element solvers

Susanne Claus, Pierre Kerfriden, Faezeh Moshfeghifar, Sune Darkner, Kenny Erleben, Christian Wong. “Contact modeling from images using cut finite element solvers” *Journal of Advanced Modeling and Simulation in Engineering Sciences*. 2021

This paper presents a robust simulation pipeline, which starts from clinical images and results in the simulation of contact between multiple bodies. The input computational models in this approach are derived from CT scans and encoded in 3D arrays of voxels. The contribution of this thesis was to provide the input data for this pipeline, which included the hip and femur surface mesh segmented from CT images.

This work was our initial attempt to use our segmented bone models for simulation purposes. The advantage of this collaboration was to pre-investigate the conventional finite element modeling workflow and figure out the existing bottlenecks in semi-automated bone segmentations. Throughout this work, we gained insights into some of the critical and labor-intensive parts of finite element modeling and identified how computer science could accelerate this approach. We have decided to exclude the manuscript of this paper from this thesis to keep the dissertation concise. We refer the reader to [4] for more details.

Appendix E

Open-Full-Jaw: An open-access dataset and pipeline for finite element models of human jaw

Torkan Gholamalizadeh, Faezeh Moshfeghifar, Zachary Ferguson, Teseo Schneider, Daniele Panozzo, Sune Darkner, Masrou Makaremi, François Chan, Peter Lampel Søndergaard, Kenny Erleben. “Open-Full-Jaw: An open-access dataset and pipeline for finite element models of human jaw” Under review at Journal of Computer Methods and Programs in Biomedicine. 2022

The contribution to this research paper is a continuation of Appendix B. We investigate the possibility of using the hip joint cartilage generation pipeline to generate discretized models of the Periodontal Ligament in the human jaw modeling application. The output of this method is both implicit representations of the PDL layer, which are suitable for simulation studies. The modeling pipeline is available on Github (<https://github.com/diku-dk/CarGen>) for public use. Figure E.1 illustrates the output results of the PDL layer. We decided to exclude the manuscript of this paper from this thesis as the rest of the paper falls out of the scope of hip joint modeling.

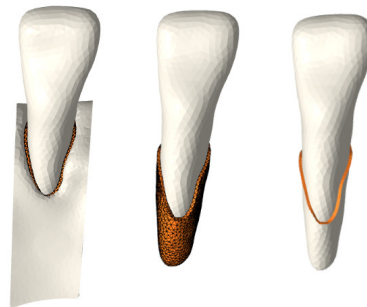


FIGURE E.1: A sample subject-specific surface mesh and the top ring of the Periodontal Ligament, residing between the teeth and the jaw.

Appendix F

Velocity Skinning for Real-time Stylized Skeletal Animation

Damien Rohmer, Marco Tarini, Niranjana Kalyanasundaram, Faezeh Moshfeghifar, Marie-Paule Cani, Victor Zordan “Velocity Skinning for Real-time Stylized Skeletal Animation” EuroGraphics. 2021

This work was a side project in my Ph.D., where we collaborated with a network of researchers from Biomechanical Modeling and Computer Graphics. This research paper has received the Honorable Mention of the Gunter Enderle Award of Eurographics 2021.

The collaboration introduced us to the essential aspects of large-scale computational modeling and was an initial attempt to apply our biomechanical point of view in a non-medical setting. The contribution to this work was mainly to feed the concepts of bone velocities to define closed-form, generic geometric deformer in cartoon animation (Figure F.1). We have decided to exclude the manuscript of this paper from this thesis as it falls out of the scope of hip joint modeling. We refer the reader to [17] for more detail.

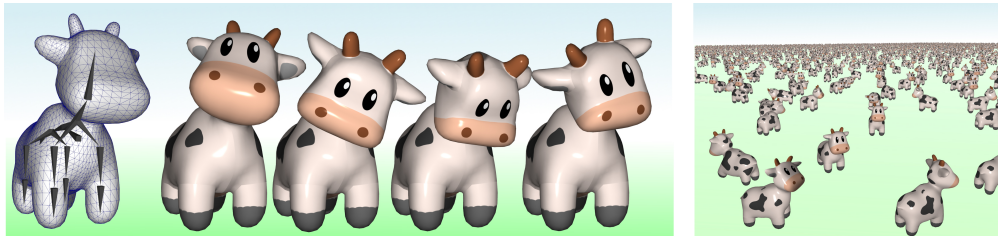


FIGURE F.1: Image taken from the paper; Left: Skeletal rig, with a single bone in the head: When animated using velocity skinning, secondary animation effects are automatically added to the ear, and face, while the horn can be set as rigid. Right: The native efficiency and simplicity of the method is compatible with GPU implementation used to compute thousands of animated cows in real-time.